Published in final edited form as:
Nature. 2021 March 01; 591(7850): 420–425. doi:10.1038/s41586-020-03166-8.

Striatal activity topographically reflects cortical activity

Andrew J Peters[1,*], **Julie MJ Fabre**[2], **Nicholas A Steinmetz**[1,2,3], **Kenneth D Harris**[2], **Matteo Carandini**[1]

[1]Institute of Ophthalmology, University College London, London, UK

[2]Institute of Neurology, University College London, London, UK

Abstract

The cortex projects to the dorsal striatum topographically [1,2] to regulate behavior [3–5], but spiking activity in the two structures has been reported to have markedly different relation to sensorimotor events [6–9]. Here we show that the relationship between activity in the cortex and striatum is spatiotemporally precise, topographic, causal, and consistent across behavioural contexts. We simultaneously recorded activity across large regions of cortex and across the width of the dorsal striatum in mice performing a visually guided task. Striatal activity followed a mediolateral gradient with behavioural correlates progressing from visual cue to response movement to reward licking. The summed activity in each part of the striatum closely and specifically mirrored activity in topographically associated cortical regions, regardless of task engagement. This relationship held for medium spiny neurons and fast-spiking interneurons, whereas tonically active neurons differed from cortical activity, responding stereotypically to sensory or reward events. Inactivation of visual cortex abolished striatal responses to visual stimuli, supporting a causal role of cortical inputs in driving striatum. Striatal visual responses were larger in trained mice than untrained mice, with no corresponding change in visual cortical fluorescence. Striatal activity therefore reflects a consistent, causal, and scalable topographic mapping of cortical activity.

The dorsal striatum serves multiple sensory [10–12], motor [13], and cognitive [14,15] roles, and receives a major synaptic input from the cortex [16,17], ordered topographically [1,2,18]. Yet, with few exceptions [19,20], recordings have suggested marked differences in sensory and behavioral correlates between striatal and cortical neurons [6–9] and between striatal cell types [7,21–23]. These differences could arise from non-cortical striatal inputs including other basal ganglia nuclei [24] and the thalamus [25,26] and from local striatal circuitry [27]. However, the possibility remains that cortex and striatum carry similar sensorimotor signals, but that this similarity is only apparent in topographically matched regions. In humans, indeed, cortical and striatal fMRI signals measured at rest are topographically correlated [28].

[*]peters.andrew.j@gmail.com .
[3]Present address: Department of Biological Structure, University of Washington, Seattle, WA

Author Contributions
AJP, KDH, and MC conceived and designed the study. AJP collected and analyzed data, JMJF analyzed cell types and single-unit data, NAS developed widefield imaging and Neuropixels setups. AJP, KDH, and MC wrote the manuscript with input from JMJF and NAS.

Competing interests
The authors declare no competing interests.

We trained mice to turn a steering wheel to move a visual grating from the periphery to the centre [29] (Fig. 1a-b). The stimulus remained fixed for 500 ms, then an auditory Go cue signaled that the stimulus position became yoked to a steering wheel and could be brought to the center to elicit a water reward (Extended Data Fig. 1a). The correct response to a stimulus on the right (contralateral to the striatal recordings) was to turn the wheel counter-clockwise, moving the stimulus from right to centre. We refer to such movements as “contralaterally-orienting”. Mice performed the task proficiently, often with fast reaction times that preceded the Go cue (Extended Data Fig. 1b-d).

While mice performed this task, we recorded activity simultaneously across the dorsal cortex and along a mediolateral trajectory spanning the dorsal striatum (Fig. 1c-d). We recorded from cortical excitatory neurons (CaMK2a tTa;tetO-GC6s transgenic mice; Ref. [30]) with widefield calcium imaging, aligning the images across sessions using vasculature and across mice using retinotopic maps (Extended Data Fig. 2). At the same time, we recorded with a Neuropixels probe [31] along the width of the striatum (n = 77 sessions across 15 mice, Fig. 1d). The probe trajectory was standardized across sessions (Extended Data Fig. 3a-b), yielding consistent electrophysiological landmarks that delimited the striatum (Extended Data Fig. 3c-d).

Progression of task-related activity

Both the cortex and striatum displayed a progression of task-related activity to visual stimuli, movement, and licking of reward (Fig. 1e-f). Following the visual stimulus, cortical activity was strongest in visual (VIS) and frontomedial regions. At the time of movement, cortical activity spread to retrosplenial (RSP) and limb somatomotor (SSp-ll, SSp-ul, posterior MOp) regions. During reward licking, activity shifted to frontolateral orofacial somatomotor regions (SSp-m, MOp, lateral MOs) (Fig. 1e). Echoing this flow of cortical activity, striatal activity progressed mediolaterally from visual stimulus to movement to licking (Fig. 1f).

Though the imaging was focused on the cortical surface, it reflected spikes in deep layers (Extended Data Fig. 4). In a subset of mice, we inserted a second Neuropixels probe in the visual cortex (n = 10 sessions across 3 mice) and determined a deconvolution kernel that optimally predicted cortical firing from widefield activity (Extended Data Fig. 4a-b). The deconvolved widefield signal correlated best with spikes in deep layers (Extended Data Fig. 4c-d), perhaps due to deep neurons’ higher firing rates and superficial apical dendrites that drive fluorescence in layer 1 [32] . Similar results were obtained with deconvolution kernels derived from only superficial or only deep spiking (Extended Data Fig. 4e).

Cortical and striatal topography

Correlations of striatal spikes at each location with cortical activity revealed an orderly progression of topographic cortical maps (Fig. 2a-e). This progression could be seen in spike-triggered averages of cortical widefield fluorescence for successively lateral striatal locations (Fig. 2a). Spike-triggered averaging, however, reflects not only interactions between signals but also autocorrelations within signals. The latter are prominent during the

task, as sensory and motor activity often overlapped. To correct for these autocorrelations, we predicted striatal spiking from cortical fluorescence using the best-fitting spatial kernels, thus obtaining a precise cortical map for each striatal location (Fig. 2b). Striatal regions along a mediolateral progression were associated with well-defined cortical regions progressing from posterior, to frontomedial, to frontolateral (Fig. 2c). Their progression was continuous (Fig. 2d), but for ease of description we grouped striatal locations into three domains: dorsomedial, dorsocentral, and dorsolateral striatum (DMS, DCS, and DLS, Fig. 2d,e). The reliable relationship of cortical and striatal activity allowed us to align striatal activity across sessions, using cortical correlations to identify striatal regions without relying on estimated coordinates.

The cortical map associated with each striatal domain was invariant to behaviour and consistent with anatomical projections (Fig. 2f-h). The cortical maps predicting activity of DMS, DCS, and DLS during task performance focused respectively on the anteromedial visual area (VISam), the frontomedial secondary motor cortex (MOs), and the frontolateral orofacial somatomotor cortex (SSp-m and Mop, Fig. 2f). Similar maps were obtained while mice passively viewed visual noise stimuli (Fig. 2g), indicating that the relationship between cortex and striatum was invariant to behavioural context. Indeed, these functional cortical maps resembled patterns of corticostriatal projections reported by the Allen Mouse Brain Connectivity Atlas [18] (Fig. 2h), suggesting that the functional relationship between cortex and striatum is primarily determined by fixed anatomical connectivity.

The relationship between striatal activity and cortical activity was stereotyped in both space and time (Fig. 2i-j). To examine the spatiotemporal association between cortical and striatal activity, we fit cortical kernels as above and allowed cortical activity a lag range of -100 to +100 ms. The resulting kernels identified a unique cortical pattern for each domain that ramped up and down in time and was weighted more strongly where cortical activity led striatal activity (Fig. 2i). These kernels were similar across sessions and behavioural context, again indicating a fixed relationship in activity between the cortex and striatum (Fig. 2j).

Striatal activity correlated best with deep cortical layers, with a latency consistent with monosynaptic connections (Extended Data Fig. 4). In the 3 mice with an additional Neuropixels probe in VISam, we compared the associated striatal activity (in DMS) with spiking across cortical layers (n = 10 sessions). Striatal activity best correlated with cortical spiking in deep layers (Extended Data Fig. 4c-f), consistent with the laminar position of corticostriatal neurons [33] . Given that cortical fluorescence also correlated best with spikes in deep cortical layers, these findings suggest that corticostriatal neurons in deep cortical layers drive the relationship between widefield cortical activity and striatal spikes (Extended Data Fig. 4d). Consistent with this hypothesis, spiking activity in the deep layers of VISam led spiking in DMS by ~3 ms, similar to measurements of corticostriatal lag [9] (Extended Data Fig. 4f).

Striatum and cortex share task responses

Firing rates in the three striatal domains reflected three task events: contralateral stimuli in DMS, contralaterally-orienting movements in DCS, and reward licking in DLS (Fig. 3a).

Ipsilateral stimuli did not evoke activity, and ipsilateral movements elicited less activity than contralateral movements (Extended Data Fig. 5a). Visual responses in DMS depended on stimulus contrast but not on the animal's upcoming choice, indicating that they encode sensory stimuli rather than action plans (Extended Data Fig. 6a). The auditory Go cue elicited activity in DMS only if mice had not already begun turning the wheel (Fig. 3a).

Firing rates in the three striatal domains were faithfully predicted from task events (Fig. 3b, c). To isolate the striatal correlates of individual task events, we fit striatal spiking as a sum of event kernels triggered on the times of stimuli of each contrast, movements in either direction, the Go cue, and rewarded and unrewarded outcomes. These event kernels described contrast-dependent contralateral stimulus responses mostly in DMS, contralaterally-biased movement responses in DCS, and reward licking responses in DLS (Fig. 3b, Extended Data Fig. 6b-c). Together, these event kernels were sufficient to predict trial-by-trial striatal activity (Fig. 3c, Extended Data Fig. 5b, cross-validated $R^2 = 0.12 \pm 0.01$ in DMS, 0.35 ± 0.02 in DCS, and 0.45 ± 0.02 in DLS, mean ± s.e. across sessions).

Remarkably, firing rates in the three striatal domains could be predicted from cortical activity despite no explicit inclusion of task events (Fig. 3d-f). We predicted firing rates in each striatal domain by applying the domain's unique spatiotemporal kernel to cortical activity (Fig. 3d). This prediction was strikingly accurate (Fig. 3a,d,e), describing trial-by-trial striatal activity as well or better than predictions from task events (Fig. 3f, cross-validated $R^2 = 0.17 \pm 0.02$ in DMS, 0.33 ± 0.03 in DCS, and 0.44 ± 0.02 in DLS, mean ± s.e. across sessions). Cortical activity was an accurate predictor of striatal activity because striatal domains and their associated cortical regions had essentially identical sensorimotor correlates (Extended Data Fig. 7a-c) that explained consistent fractions of variance across two structures (Extended Data Fig. 7d). Good predictions of striatal firing were only possible from a domain's associated cortical regions, not from other cortical regions or other striatal domains (Extended Data Fig. 8a).

Striatal activity topographically mirrored the associated cortical regions not only during the sensorimotor task, but also while mice were passive outside the task (Extended Data Fig. 8b-e). When mice passively viewed visual noise stimuli, the visual cortex and DMS exhibited oscillating, synchronous activity [34], while the DCS and DLS were less active due to reduced movement (Extended Data Fig. 8b). Despite these contextual differences in striatal activity, cortical activity predicted striatal firing as well as during task performance, explaining slightly more variance in DMS and slightly less in DCS and DLS (Extended Data Fig. 8c). These slight differences were consistent with the changes in variance between task and rest (Extended Data Fig. 8d), with the amount of striatal activity explained by cortex limited only by the variance present to explain (Extended Data Fig. 8e).

The close match between cortical and striatal activity suggests that the striatum inherits its task responses from the cortex, a hypothesis that was supported by inactivation experiments (Fig. 3g, Extended Data Fig. 9). In six of the mice we performed our simultaneous cortical and striatal measurements before and after inactivation of VISam with topical muscimol. Cortical muscimol effectively silenced spiking in all layers of cortex (Extended Data Fig. 9a). When applied over VISam it strongly reduced local visual responses (Extended Data

Fig. 9b). Cortical muscimol slightly increased the average striatal firing rate (Extended Data Fig. 9c), but reduced visual responses in DMS (Fig. 3g) proportionally to the reduction in VISam (Extended Data Fig. 9d). During task performance, cortical muscimol increased reaction times and increased contralaterally orienting responses particularly at low ipsilateral contrasts, suggesting that mice used only the ipsilateral stimuli to guide movements, defaulting to the contralateral side when the ipsilateral stimulus was not perceived (Extended Data Fig. 9e). Fitting task event kernels to neural activity revealed that VISam inactivation selectively eliminated striatal visual responses, sparing activity related to movement and reward licking (Extended Data Fig. 9f). These results indicate that, at least for visual responses, striatal firing requires propagation of activity from the associated cortical region.

Striatal cell type activity

The match between striatal activity and topographically associated cortex held for putative medium spiny neurons (MSNs) and putative parvalbumin-positive [35] fast-spiking interneurons (FSIs), but not for putative cholinergic [36] tonically active neurons (TANs), which had strikingly different and stereotyped activity (Fig. 4). MSNs constitute 95% of striatal neurons, and the rest are interneurons which have been proposed to have unique responses [7,21,22] . To examine their task-related activity, we selected high-quality single units (8,303/21,047) and used electrophysiological criteria [37,38] to group them into MSNs, FSIs, and TANs (Fig. 4a), plus a separate a class of unidentified interneurons [37] (UINs) (Extended Data Fig. 10). MSNs fired at a range of different times associated with stimulus, movement and reward licking (Fig. 4b, **left**). The proportion of cells responding to these events differed across domains: nearly all stimulus-responsive cells were in DMS, most movement-onset responsive cells in DCS, and most licking-responsive cells in DLS. Averaging MSN activity in each domain yielded a multiunit signal that mirrored activity in the topographically associated regions of cortex (Figure 4c, **left**). Surprisingly given previous reports [7,22,39] , FSI activity resembled MSNs, albeit with higher firing rates (Fig. 4b and c, **centre**). In contrast, TANs had different activity: they responded synchronously with a burst followed by a pause following the stimulus (in DMS and DCS) or reward licking (in DCS and DLS), respecting an unexpected [40,41] segregation according to striatal domain (Fig. 4b and c, **right**).

These results suggest that while MSNs and FSIs are similarly driven by cortical activity, TANs are more independent, consistent with their weaker cortical input [42] . To quantify these effects, we correlated the activity of individual striatal neurons with the summed activity of each cell type in their domain, and with cortical widefield in the associated region. MSNs and FSIs showed similar correlation with the activity of either class and with topographic cortical activity, but low correlation with TAN activity (Fig. 4d, **left and centre**). In contrast, TAN activity correlated strongly with other TANs, but weakly with other cell types or with cortex (Fig. 4d, **right**).

Training striatal sensory responses

Training in the task increased DMS sensory responses in both MSNs and TANs but not in FSIs (Fig. 5). We compared responses to visual stimuli in untrained mice (n = 23 sessions, 5 mice) and in trained mice while in a passive context (n = 48 sessions in 11 mice), excluding

trials with wheel movements. Cortical responses in VISam were similar in untrained and trained mice (Fig. 5a). By contrast, trained mice had larger visual responses in DMS (Fig. 5b). This increase affected MSNs and TANs but not FSIs, suggesting a differential effect of training across cell types (Fig. 5c). Training also gave rise to stimulus responses in DCS (Fig. 5b-c), which were likely inherited from training-induced stimulus responses in the associated frontomedial cortex [43] (Fig. 5a, **middle**). Nonetheless, cortical kernels for each striatal domain had consistent topography and time course across trained and untrained mice (Fig. 5d), indicating that the spatiotemporal relationship between the cortex and striatum is consistent, with a gain that changes across learning.

Discussion

These results establish that summed activity in each striatal domain causally reflects summed activity in the topographically associated cortical region, independent of behavioral context but scaled by learning. These results contrast with previous studies, which suggested marked differences between cortical and striatal activity [6–8] and between MSN and FSI activity [7,22] , possibly due to the difficulty in precisely matching associated cortical and striatal regions and consistently recording in the same striatal locations.

Our data suggest that associated regions of cortex and basal ganglia form a continuously cooperative circuit that is active throughout sensation and movement rather than just at event onsets and offsets [44] . This circuit may link stimuli to actions [5,15] and continuously modulate behavior [13,20,39] . Striatal activity is also likely to reflect non-cortical inputs from the amygdala, hippocampus, and thalamus [2] . Indeed, the thalamus provides almost half of all excitatory synapses to the striatum [17] , and dominates the inputs to TANs [42] , potentially explaining their difference from cortical activity.

Our data also indicate that while the overall transfer function from the cortex to the striatum is stable, its gain is scalable with learning. This gain change operates at the level of summed activity; individual MSNs showed diverse activity correlates, and their learning-related plasticity may also be diverse or different across direct and indirect MSNs [45] . Our results are consistent with reports that learning strengthens corticostriatal synapses [45–47] and correlations [20,48] , and suggest that cortical activity may most effectively propagate to the striatum when it has been learned as behaviorally relevant. Notably, no gain change was seen in FSIs, possibly reflecting a learning-independent role of these neurons in regulating MSN activity [49] .

Overall, there is a remarkably close relationship between cortical and striatal activity, which is largely determined by topography and invariant to context. Cortical signals are faithfully reflected in striatum, and are therefore poised to determine further processing as activity propagates through the basal ganglia to determine behavior.

Methods

All experiments were conducted according to the UK Animals (Scientific Procedures) Act 1986 under personal and project licenses issued by the Home Office.

Animals

Mice were adult (6 weeks or older) male and female transgenic mice (TetO-G6s;Camk2a-tTa, Ref. [30]) which did not show evidence of epileptiform activity [50].

Surgery

Two surgeries were performed for each animal, the first for headplate implantation and widefield imaging preparation, and the second for a craniotomy for acute electrophysiology. Mice were anesthetized with isoflurane, injected subcutaneously with caprofen, and placed in a stereotaxic apparatus on a heat pad. The head was then shaved, the scalp cleaned with iodine and alcohol, and the scalp was removed to expose the skull. The cut skin was sealed with VetBond (World Precision Instruments), the skull was scraped clean and a custom headplate was fixed to the interparietal bone with dental cement (Super-Bond C&B). A plastic 3D-printed U-shaped well was then cemented to enclose the edges of the exposed skull. A layer of VetBond or Zap-A-Gap (Pacer Technology) was applied to the skull followed by two layers of UV-curing optical glue (Norland Optical Adhesives #81, Norland Products). Caprofen was added to the drinking water for 3 days after surgery. For electrophysiological recordings, on the first day of recording mice were anesthetized and a 1mm craniotomy was drilled or cut with biopsy punch approximately 200 μm anterior and 1000 μm lateral to bregma. The craniotomy was then covered with Kwik-Cast (WPI) and mice were given hours to recover before recording. Craniotomies were covered with Kwik-Cast between days.

Visually guided wheel-turning task

The task is described in detail elsewhere [29]. It was programmed in Signals, part of the Rigbox MATLAB package [51]. Mice were trained on a 2-alternative forced choice task requiring directional forelimb movements to visual stimuli (Fig. 1, Extended Data Fig. 1a). Mice were headfixed and rested their body and hindpaws on a stable platform and their forepaws on a wheel that was rotatable to the left and right. Trials began with 0.5 s of enforced quiescence, where any wheel movements reset the time. A static vertical grating stimulus then appeared 90° from centre with a gaussian window $\sigma = 20°$, spatial frequency 1/15 cycles/degree, and grating phase randomly selected on each trial. After 0.5 s from stimulus onset, a Go cue tone (12 kHz, 100 ms) sounded and the position of the stimulus became yoked to the wheel position (e.g. leftward turns moved the stimulus leftward). Mice usually began turning the wheel before the Go cue even on trials with 0% contrast (invisible) stimuli (Extended Data Fig. 1c), indicating a rapid decision process and expected stimulus time, although as the session progressed and mice became sated they began waiting for the Go cue more often (Extended Data Fig. 1d). Bringing the stimulus to the centre (correct response) locked the stimulus in the centre for 1 s and 2 μL of water was delivered from a water spout near the mouse's mouth, after which the stimulus disappeared and the trial ended. Alternately, moving the stimulus 90° outward (incorrect response) locked the stimulus in place off-screen and a low burst of white noise played for 2 s, after which the trial ended. The stimulus contrast varied across trials taking the values of 0%, 6%, 12.5%, 25%, 50%, or 100%. Difficulty was modulated with an alternating staircase design, where even trials used a random contrast, and odd trials followed a staircase that moved to a lower

contrast after 3 correct responses and moved to higher contrast after 1 incorrect response. Correct responses on high-contrast trials were encouraged by immediately repeating all incorrect trials with 50% or 100% contrast, but these repeated trials were excluded from all analyses. Other than repeat trials, stimulus side was selected randomly on each trial. Mice were trained in stages, where first they were trained to ~70% performance with only 100% and 50% contrast trials, then lower contrasts were progressively and automatically added as performance increased. Imaging sessions began after all contrasts had been added, and simultaneous imaging and electrophysiology sessions began after ~4 days of imaging-only sessions.

Widefield imaging and fluorescence processing

Widefield imaging was conducted with a sCMOS camera (PCO Edge 5.5) affixed to a macroscope (Scimedia THT-FLSP) with a 1.0x condenser lens and 0.63x objective lens (Leica). Images were collected with Camware 4 (PCO) and binned in 2x2 blocks giving a spatial resolution of 20.6 μm/pixel at 70 Hz. Illumination was generated using a Cairn OptoLED with alternating blue (470 nm, excitation filter ET470/40x) and violet (405 nm, excitation filter ET405/20x) light to capture GCaMP calcium-dependent fluorescence and calcium-invariant hemodynamic occlusion respectively at 35 Hz per light source. Illumination and camera exposure were triggered externally (PCIe-6323, National Instruments) to be on for 6.5 ms including a 1 ms illumination ramp up and down time to reduce light-induced artifacts on the Neuropixels probe. Excitation light was sent through the objective with a 3mm core liquid light guide and dichroic (387/11 single-band bandpass) and emitted light was filtered (525/50-55) before the camera.

To reduce data size for storage and ease of computation, widefield data was compressed using singular value decomposition (SVD) of the form $\mathbf{F} = \mathbf{USV}^{\mathbf{T}}$. The input to the SVD algorithm was **F**, the *pixels* × *time* matrix of fluorescence values input to the SVD algorithm; the outputs were **U**, the *pixels* × *components* matrix of template images; **V** the *time* × *components* matrix of component time courses; and ***S*** the diagonal matrix of singular values. The top 2000 components were retained, and all orthogonally-invariant operations (such as deconvolution, event-triggered averaging and ridge regression to predict striatal activity from the widefield signal) were carried out directly on the matrix **S** * **V**, allowing a substantial saving of time and memory.

Hemodynamic effects on fluorescence were removed by regressing out the calcium-independent signal obtained with violet illumination from the calcium-dependent signal obtained with blue illumination. To do this, both signals were bandpass filtered in the range 7-13 Hz (heartbeat frequency, expected to have the largest hemodynamic effect), downsampling the spatial components 3-fold, and reconstructing the fluorescence for each downsampled pixel. Pixel traces for blue illumination were then temporally resampled to be concurrent with violet illumination (since colours were alternated), and a scaling factor was fit across colours for each pixel. The scaled violet traces were then subtracted from the blue traces.

To correct for slow drift, hemodynamic-corrected fluorescence was then linearly detrended, high-pass filtered over 0.01 Hz, and ΔF/F0 normalized by dividing by the average fluorescence at each pixel softened by adding the median average fluorescence across pixels.

Widefield images across days for each mouse were aligned by rigid registration of each day's average violet-illumination image which was dominated by vasculature (Extended Data Fig. 2a). Widefield images across mice were aligned by affine alignment of average visual field sign maps for each mouse (Extended Data Fig. 2b-c). The Allen Common Coordinate Framework [52] (CCF v3, © 2015 Allen Institute for Brain Science. Available from: download.alleninstitute.org/informatics-archive/current-release/mouse_ccf/) atlas was aligned to the grand average and symmetrized sign map across mice by assigning expected visual field sign to visual areas [53] and affine aligning the annotated CCF to the average sign map (Extended Data Fig 2d). Even though CCF alignment was done using posterior visual areas, it was successful in aligning the entire brain as evidenced by correspondence between correlated widefield regions and CCF borders (Extended Data Fig. 2e-f) and the ability to accurately estimate anterior probe trajectories from widefield images (Extended Data Fig. 3a).

To combine SVD-compressed widefield data across recordings, data was recast from experiment-specific SVD components into a master SVD basis set. These master SVD components were created by aligning and concatenating components **U** from the last imaging-only session of all animals (i.e. no craniotomy), performing an SVD on that concatenated matrix, and retaining the top 2000 components to serve as the master SVD components. Temporal components (**S * V**) for each experiment were recast by

$$\mathbf{S} * \mathbf{V}_{\text{master}} = \mathbf{U}_{\text{master}}^{T} * \mathbf{U}_{\text{experiment}} * \mathbf{S} * \mathbf{V}_{\text{experiment}}$$

Fluorescence was deconvolved using a kernel fit from predicting cortical multiunit activity from widefield GCaMP6s fluorescence. This kernel was estimated using data from simultaneous widefield imaging and Neuropixels recordings in the visual cortex (Extended Data Fig. 4a-b, with the final deconvolution kernel being a mean of max-normalized kernels across recordings divided by the sum of squared weights across time. The deconvolution kernel was biphasic and roughly similar to a derivative filter (i.e. [-1,1]) (Extended Data Fig. 4b), consistent with rises in the GCaMP signal correspond to periods of spiking.

Retinotopic mapping

Cortical visual areas were mapped using visual sparse noise stimuli which also provided the "passive context" in our analyses. White squares 7.5° in length were presented asynchronously on a black background, with each square lasting 166 ms and ~12% of squares being present at any given time. Activity for each square presentation was averaged within a 300-500 ms time window (corresponding to the maximum GCaMP6s signal), and the average response to each square was bootstrapped 10 times. Visual field sign maps (Extended Data Fig. 2b) were calculated for each bootstrapped mean and then averaged. Visual field sign was defined by gaussian-smoothing average square responses, finding the center-of-mass for each cortical pixel relative to the square azimuth and elevation locations,

determining the gradient within these azimuth and elevation center-of-mass maps, and taking the sine of the difference between the azimuth and elevation gradients.

Neuropixels recordings

Electrophysiological recordings were made with Neuropixels Phase 3A probes [31] affixed to metal rods and moved with micromanipulators (Sensapex). Raw data within the action potential band (soft high-pass filtered over 300 Hz) was de-noised by common mode rejection (i.e. subtracting the median across all channels), and spike-sorted using Kilosort 2 (www.github.com/MouseLand/Kilosort2). Units representing noise were manually removed using Phy [54] . Multiunit activity was then defined as spikes pooled from all Kilosort-identified units within a given segment of the probe.

Electrophysiological recordings were synchronized to widefield data and task events by aligning to a common digital signal randomly flipping between high and low states (produced from an Arduino) accounting for both clock offset and drift.

Light from the LED used during widefield imaging produced a substantial artefact in the electrophysiological data. This artefact was reduced by ramping the light over 1ms, and was removed from the action potential band by subtracting the average signal across all channels. Kilosort occasionally identified units from a small remaining artefact which were readily identifiable from their shape and regularity and were discarded. The light artefact was removed from the LFP band (used in Extended Data Fig. 4c) by subtracting a rolling median light-triggered average for each LED colour.

Probe trajectories were reconstructed from histology (Extended Data Fig. 3a) using publicly available custom code (github.com/petersaj/histology). Probe trajectories were estimated from widefield images (Extended Data Fig. 3b) by manually identifying the probe in the image and transforming the location into CCF coordinates using the retinotopy-CCF alignment for that recording.

Striatal electrophysiology and depth-alignment

For striatal recordings, probes were inserted at approximately 200 μm anterior and 1000 μm lateral to bregma at a 45° angle from horizontal (diagonally downwards) and 90° from the anterior-posterior axis (straight coronally) to a depth of ~6 mm along the probe axis to reach the contralateral striatum. Electrophysiological data was recorded with Open Ephys [55] .

The borders of the striatum were identified within each recording using the ventricle and dorsolaterally-neighbouring structure (endopiriform nucleus or claustrum) as electrophysiological landmarks. Since no units were detected in the ventricle, the start of the striatum on the probe was marked as the first unit after at least a 200 μm gap from the last unit (or the top of the probe if no cortical units were detected). Detected units were continuous after the ventricle, but multiunit correlation in temporal bins of 10 ms and sliding spatial bins of 100 μm revealed a sharp border in correlation at a location consistent with the end of the striatum (Extended Data Fig. 3d). This lateral border of the striatum was present in every recording and used to define the end of the striatum on the probe.

Striatal recordings were aligned by depth using the lateral striatal border, as the lateral border was sharp while the medial border was inferred from lack of units and therefore imprecise. The location of striatal units was then defined as distance from the lateral border, and depth-aligned analyses were performed on these distances divided into ~200 μm segments (Fig. 1f, Fig. 2a-b). Only depths present in > 50% of recordings are shown, eliminating a sparse subset of medial depths in recordings with an unusually large portion of the probe corresponding to the striatum. Note that aligning by depth is only approximate, while aligning by functionally associated cortical maps provides a much more precise method of alignment (below).

Single-unit analysis and striatal cell-type classification

High-quality single units were defined by the following criteria:

1. Waveform trough to peak amplitude of more than 77 μV (based on a distribution of amplitudes)
2. Minimum of 300 spikes
3. Less than 30% of spikes missing, estimated by fitting a gaussian to the spike amplitude distribution with an additional cut-off parameter below which no spikes are present (using the Python function scipy.optimize.curve_fit)
4. Waveform trough that preceded a waveform peak, to eliminate axonal spikes [56].
5. An estimated false-positive rate of less than 10% using the approach of Ref. [57]. This estimates the false-positive rate F_p as the solution to

$$r = 2(\tau_R - \tau_C)N^2(1 - F_p)F_p/T$$

Where r is the number of refractory period violations; τ_R the refractory period (taken as 2 ms), τ_c the censored period (taken as 0.5 ms), τ_c the number of spikes, F_p the false positive rate, T the total recording time. MATLAB's built-in function roots was used for this. If an imaginary number was returned by the function, due to r being too high, the F_p rate was set to 1 as in Ref. [57], and the unit rejected.

Units passing these quality criteria were then classified into four putative striatal cell types: medium spiny neurons (MSNs), fast-spiking interneurons (FSIs), tonically-active neurons (TANs) and a fourth class of unidentified interneurons (UINs) (Extended Data Fig. 10). Neurons with narrow waveforms (Kilosort template trough-to-peak waveform duration <= 400 μs) were identified as either FSIs or UINs as in Ref. [37]. Putative FSIs and UINs were then separated using the proportion of time associated with long interspike intervals (ISIs >2 s) by summing ISIs longer than 2 s and dividing the sum by the total recording time (as calculated in Ref. [38]): neurons where this ratio was more than 10% were classified as UINs, and the others as FSIs. The remaining units were presumed to be TANs and MSNs, which were further separated using the post-spike suppression. We measured the length of time that a unit's firing rate was suppressed following an action potential by counting the number of 1ms bins in its autocorrelation function until the unit's firing rate was equal or greater to

its average firing rate over the 600 ms to 900 ms autocorrelation bins. Units with post-spike suppression of > 40 ms were labelled TANs, and the remaining units were labelled MSNs. A few units had short waveforms (< 400 μs) and long post-spike suppression (> 40 ms). These units were very rare (36/8,303) and exhibited TAN-like responses and might therefore be TAN neurites; they were excluded from further analysis.

Cortical electrophysiology and alignment

For cortical recordings, a second craniotomy was performed over VISam targeted by retinotopic visual field sign maps relative to vasculature. During recording, a second Neuropixels probe was inserted into VISam at a 45° angle from horizontal (diagonally downwards) and 90° from the anterior-posterior axis (straight coronally) to a depth of ~2 mm along the probe axis.

Cortical depth was aligned across recordings using current source density (CSD) analysis. Mice were passively presented with visual gratings, and the CSD was computed as the second spatial derivative of the stimulus-triggered average LFP signal, smoothed by a boxcar rolling average of 10 channels. The average CSD 40-60 ms after the stimulus was then aligned across recordings by interpolation using the maximum sink (Extended Data Fig. 4c, red patch) and the first source (Extended Data Fig. 4c, top blue patch). The “aligned visual cortex depth” (Extended Data Fig. 4c) was then set relative to these points, with the first source being 0 and the maximum sink being set to the median source-sink distance across sessions. Superficial and deep layers were defined as being above or below midway from the sink to the lower source (Extended Data Fig. 4c, horizontal line). The ventral border of the cortex was made clear by a gap in detected units corresponding to the white matter.

Regression from task events to activity

Regression from task events to striatal multiunit activity or deconvolved cortical fluorescence activity was performed using linear regression of the form

$$\begin{pmatrix} F_{t1} \\ \vdots \\ F_{tn} \end{pmatrix} \sim \begin{pmatrix} Task\ event_{\ event\ 1,\ time\ lag\ 1,t1} & \cdots & Task\ event_{\ event\ n,time\ lag\ n,timepoint\ 1} \\ \vdots & \ddots & \vdots \\ Task\ event_{\ event\ 1,\ time\ lag\ 1,\ tn} & \cdots & Task\ event_{\ event\ n,time\ lag\ n,timepoint\ n} \end{pmatrix} * K_{task\ ®\ activity}$$

Here, $K_{task \rightarrow activity}$ represents a vector containing the concatenated estimated kernels for each event type, estimated by least squares using MATLAB’s \ operator. F_{t1} to F_{tn} represent the fluorescence or firing rate time course to be predicted, “baseline-subtracted” by subtracting the average combined activity - 0.5-0 s before all stimulus onsets, during which times the animals were required not to turn the wheel. For each event type, a task matrix was constructed as a sparse Toeplitz matrix with a diagonal series of 1’s for each event at each time lag, with zeros elsewhere. Toeplitz matrices were made for each event type: stimulus onset (one for each stimulus side*contrast, lags of 0-0.5 s), movement onset (one each for left and right final response, lags of -0.5-1 s), go cue onset (one for trials where mice had already begun moving and one for trials with no movement before the go cue, lags of 0-0.5 s), and outcome (one for water and one for white noise, lags of 0-0.5 s). These matrices were

horizontally concatenated to produce the matrix shown in the above equation. Regression was 5-fold cross-validated by splitting up timepoints into consecutive chunks.

Regression from cortical activity to striatal activity

Normalized, hemodynamically-corrected, and deconvolved widefield fluorescence was regressed to striatal multiunit activity using ridge regression. Regression took the form

$$\begin{pmatrix} F_{t1} \\ \vdots \\ F_{tn} \\ 0 \\ \vdots \\ 0 \\ 0 \end{pmatrix} \sim \begin{pmatrix} SV\ component\ 1, time\ lag\ 1, timepoint\ 1 & \cdots & SV\ component\ n, time\ lag\ n, timepoint\ 1 & 1 \\ \vdots & \ddots & \vdots & \vdots \\ SV\ component\ 1, time\ lag\ 1, timepoint\ n & \cdots & SV\ component\ n, time\ lag\ n, timepoint\ n & 1 \\ \lambda & 0 & 0 & 0 \\ \vdots & \ddots & \vdots & \vdots \\ 0 & 0 & \lambda & \vdots \\ 0 & 0 & 0 & 0 \end{pmatrix} * K_{cortex \circledR striatum}$$

Here, F_{t1} to F_{tn} represent the standard-deviation-normalized striatal spiking time course to be predicted. $K_{cortex \rightarrow striatum}$ represents the estimated spatiotemporal kernel from cortical fluorescence to standard-deviation-normalized striatal spiking estimated by least squares using MATLAB's \ operator. To make the design matrix, a Topelitz matrix was constructed for each temporal SVD component of the cortical widefield, scaled by the singular values (S*V), staggered across a range of time values (-100 ms to +100 ms). These Toeplitz matrices were horizontally concatenated, also including a column of ones to allow an offset term. To regularize using ridge regression, this matrix was vertically concatenated above diagonal matrix of regularization values λ, and the striatal activity time courses F were concatenated above the same number of zeros. Regression was 5-fold cross-validated by splitting up timepoints into consecutive chunks, and values for λ were determined empirically for each experiment by regressing from cortical fluorescence to multiunit from the whole striatum across a range of λ values and finding the λ that yielded the largest cross-validated explained variance.

Striatal domain assignments

Striatal domains were defined from cortical maps as spatial kernels (time lag = 0) described above for consecutive 200 μm segments of the Neuropixels track through the striatum recorded in each experiment. The cortical maps were combined across all sessions and animals and split into 3 groups through K-means, and the average cortical map for each group was used as a template for each striatal domain. The spatial map from each 200 μm striatal segment was then assigned to one group by highest correlation with the template maps. Striatal domain assignments were smoothed using a 3-segment median filter and restricted to a standard order by replacing mis-ordered assignments with their nearest neighbour. This process ensured contiguous domains and was empirically successful at removing rare aberrations. Our dorsomedial, dorsocentral, and dorsolateral domains approximately correspond to the medial dorsomedial subdivision, lateral dorsomedial subdivision, and dorsolateral domains of Hunnicutt et al. [2] and the domains i.dm.d/dm/im, i.dm.cd/i.vl.cvl, and i.vl.v/vt in Hintiryan et al. [1] .

Europe PMC Funders Author Manuscripts

Multiunit activity for each domain and session was created by pooling all spikes within striatal segments assigned to a given domain. Multiunit activity was expressed as ΔFR/FR0, being the firing rate baseline-subtracted (average from 0.5-0 s before stimulus onset in each trial) and divided by the average firing rate across all baseline timepoints plus a 10 spikes/s softening factor.

Cortical regions-of-interest for striatal domains

Cortical regions-of-interest (ROIs) corresponding to the most correlated cortical region for each striatal domain (used in Fig. 4c-d, Fig. 5a, Extended Data Fig. 9d) were generated using the template cortical map for each domain described above. Pixels were thresholded above 75% of the maximum weighted pixel and contralateral pixels and clusters smaller than 100 pixels were removed, resulting in a discrete cortical ROI over the region most correlated with each striatal domain.

Allen connectivity maps

Anatomical projections were labelled using the Allen Mouse Brain Connectivity Atlas [18] (Fig. 2h, © 2015 Allen Institute for Brain Science. Allen Brian Atlas API. Available from: brain-map.org/api/index.html) was queried for injection sites within the cortex that yielded axon terminals in each striatal domain, and the seed points used for each striatal domain were the centre-of-mass for each domain relative to the longest recorded striatal length and interpolated into the targeted striatal trajectory in the CCF atlas (shown in Fig. 2e). To maximize coverage across the brain since the Allen Mouse Brain Connectivity Atlas has different left and right hemisphere injections, queries were performed for striatal sites bilaterally and results from the right striatum were mirrored and combined with the results from the left striatum. The cortical sites with striatal projections returned by the API were then plotted as a heatmap by binning across space and blurring with a gaussian filter.

Muscimol experiments

For inactivation experiments, in the same surgery that placed a craniotomy with access to the striatum, a second craniotomy was performed over VISam targeted by retinotopic visual field sign maps relative to vasculature. During the experiment, mice performed the task for approximately half of the normal number of trials and were then shown visual noise stimuli and passive gratings. Muscimol (Sigma, 5 mM in ACSF) was then applied topically by placing muscimol-soaked gelfoam in the VISam craniotomy for 40 minutes, with additional ACSF applied at 20 minutes to prevent drying. Mice then performed the task until they no longer engaged and were again shown visual noise stimuli and passive gratings.

The effect of topical muscimol by cortical depth was assessed in two separate mice (Extended Data Fig. 9a) by inserting a Neuropixels probe near the edge of a craniotomy and recording activity before and after muscimol application.

In sessions with cortical inactivation, mice performed the task as described above without the inclusion of repeat trials for incorrect 50% and 100% contrast stimuli described above. This was normally included to discourage bias and was excluded in these sessions to allow for a muscimol-induced bias.

Europe PMC Funders Author Manuscripts

Extended Data

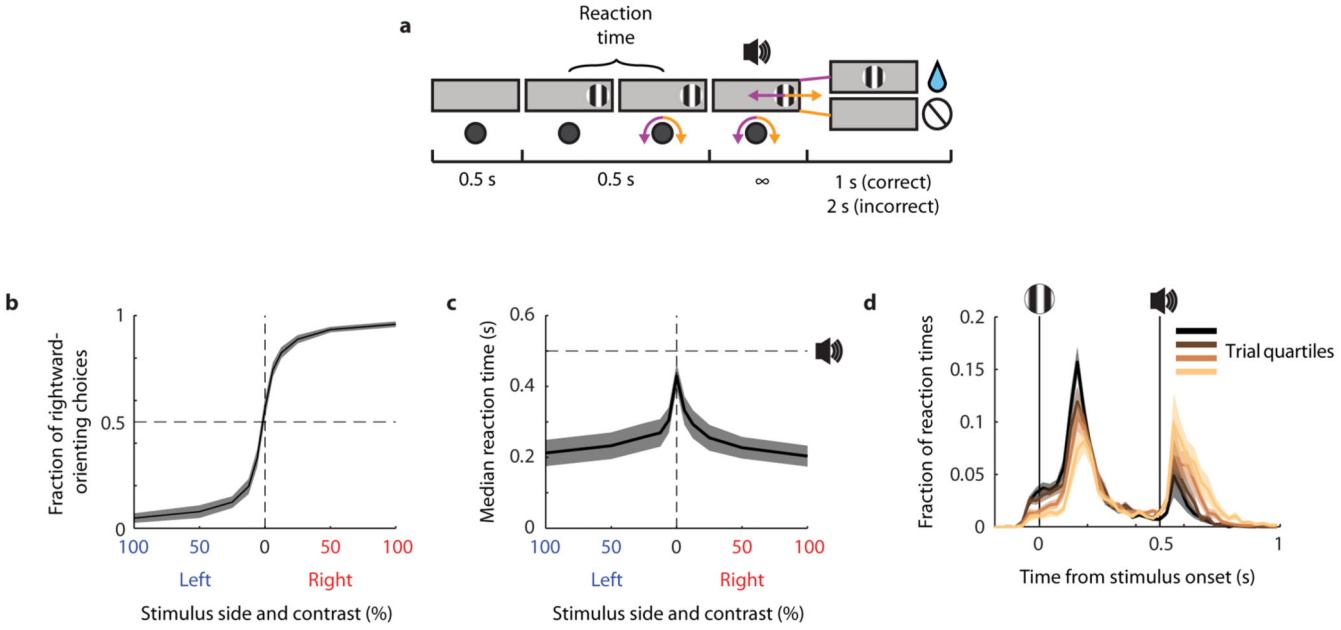

Extended Data Fig. 1. Task performance.

a, Timeline of events in a trial. After 0.5 s with no wheel movement, a stimulus appears. The mouse may turn the wheel immediately, but it only becomes yoked to the stimulus after a further 0.5 s, at which time an auditory Go cue is played. If the mouse drives the stimulus into the centre, a water reward is delivered and a new trial begins after 1s; if the mouse drives the stimulus off the screen away from the centre, a white noise sound is played and a new trial begins after 2 s. **b**, Psychometric curve showing task performance: the fraction of choices as a function of stimulus contrast and side. Curve and shaded region show mean ± s.e. across sessions. **c**, Median reaction time as a function of stimulus contrast and side as in (b) (mean ± s.e. across each session's median). Dotted horizontal line indicates time of auditory Go cue. **d**, Histogram of times from stimulus to movement onset (reaction time) by trial quartile within sessions (first quarter of trials in the session in black, last quarter in beige; mean ± s.e. across mice). In early trials, mice typically begin moving the wheel before the Go cue. Later in the sessions, they waited more often for the Go cue.

Europe PMC Funders Author Manuscripts

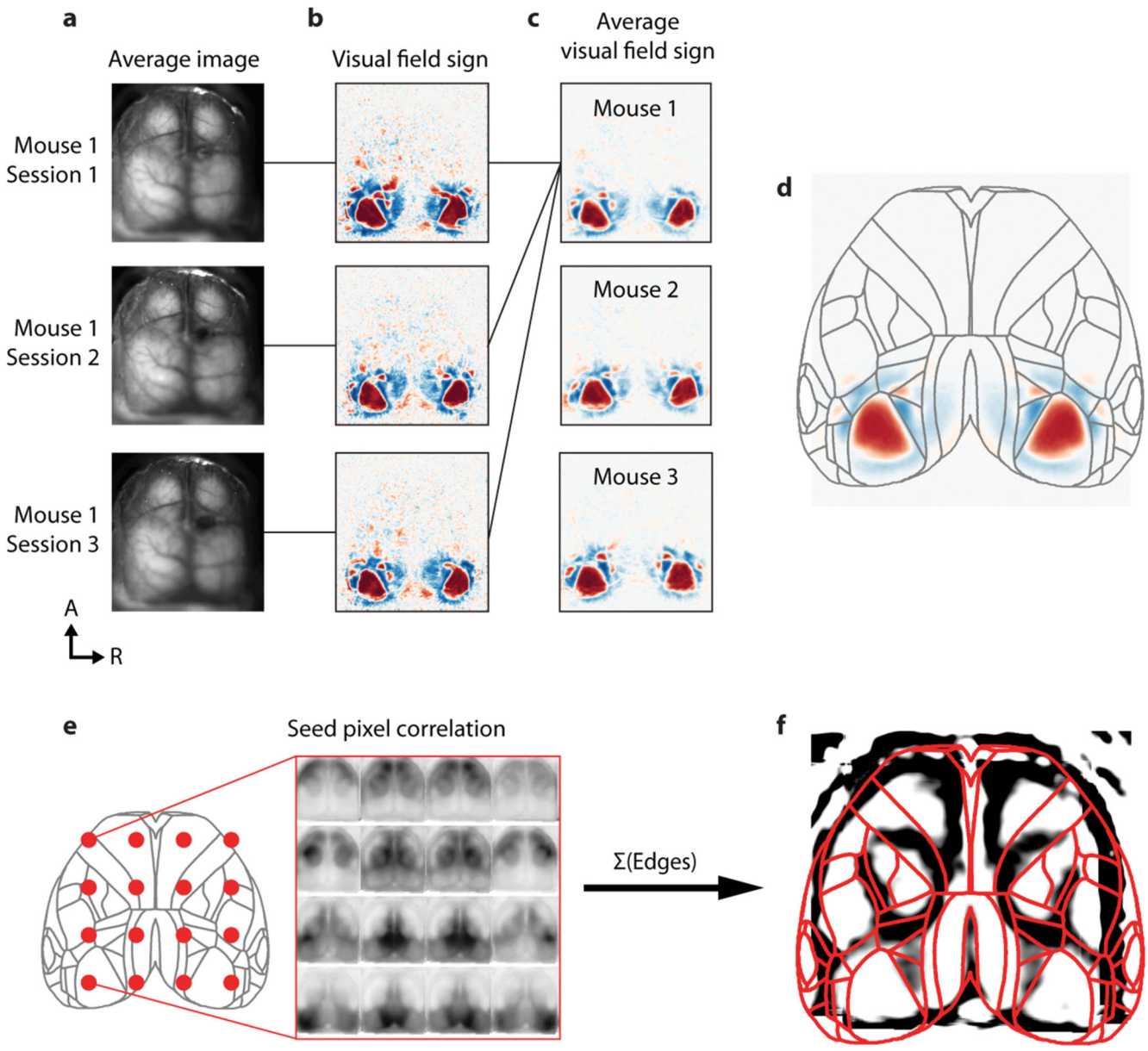

Extended Data Fig. 2. Cortical widefield alignment.

a, Example widefield images from one mouse, used to align vasculature. **b**, Retinotopic visual field sign maps corresponding to the sessions in (a). **c**, Retinotopic maps averaged across all sessions for three example mice, used to align widefield images across mice. **d**, Retinotopic map averaged across mice and symmetrized, used to align widefield images to the Allen CCF atlas (used only for figure overlay purposes). **e**, Cortical seed pixels (left) and corresponding pixel-pixel correlation maps (right). Each pixel-pixel correlation map (right) is made by correlating a given pixel with all other pixels, which reveals clusters of pixels belonging to correlated cortical regions (e.g. the central circles corresponding to limb somatomotor cortex). **f**, Summed edge-filtered pixel-pixel correlation maps (as in e) showing the outlines of correlated clusters of pixels. Each pixel-pixel correlation map (as

in e) highlights a correlated cluster of pixels. Edge-filtering each pixelpixel correlation map then draws a boundary around the highlighted correlated cluster. Summing these edges across all pixel-pixel correlation maps illustrates the boundaries of all correlated clusters of pixels, prominently including limb somatomotor cortex (central circles), visual cortex (posterior lateral triangular regions), retrosplenial cortex (posterior medial region), and orofacial somatomotor cortex (frontal lateral regions). The Allen CCF regions aligned using retinotopy (*red*) align well to correlation borders, indicating that our alignment methods based on posterior retinotopy also successfully align anterior regions.

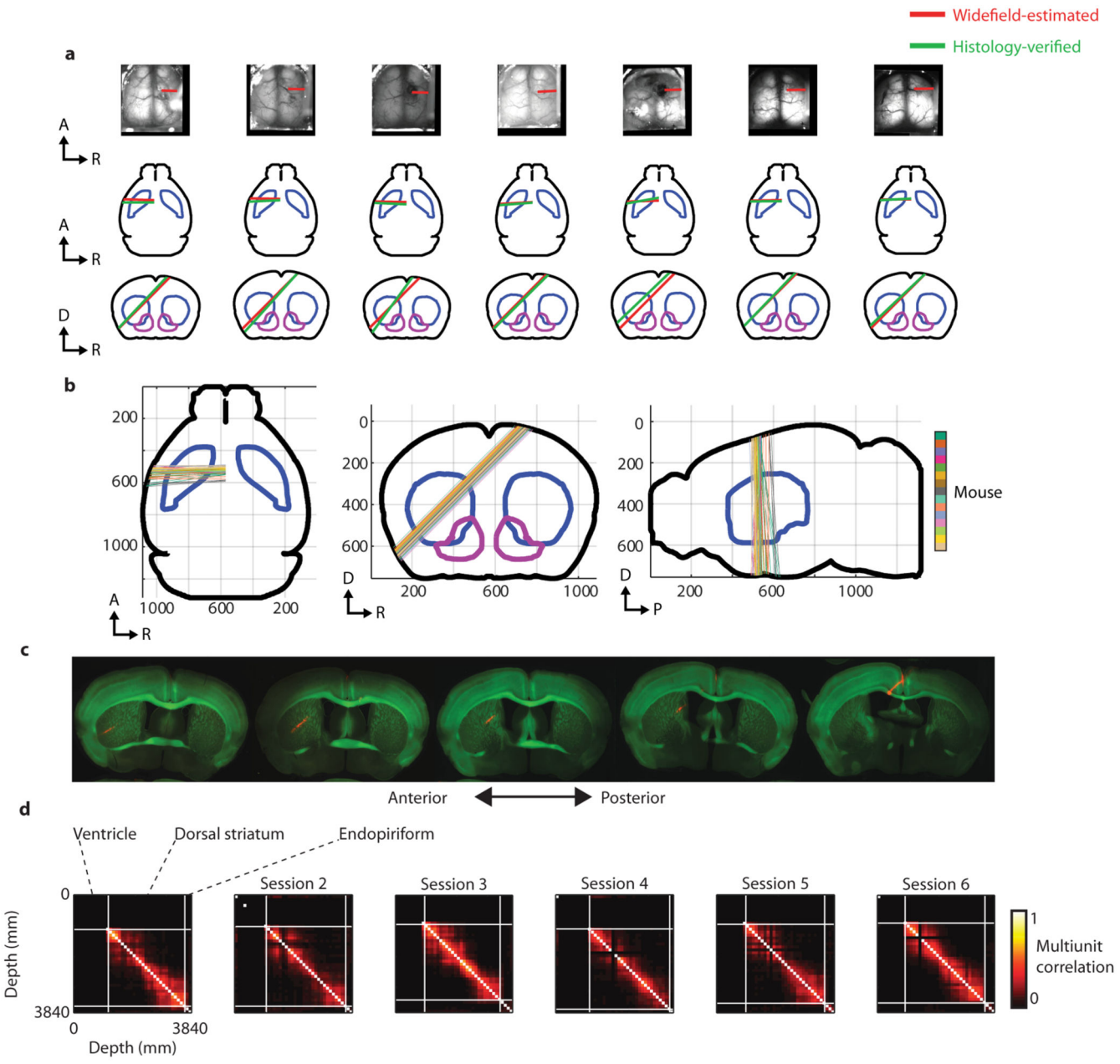

Extended Data Fig. 3. Striatal recording locations and electrophysiological borders.

a, Top, widefield images used to approximate probe location (*red line*); middle/bottom, horizontal and coronal views of the brain with widefield-estimated probe location (*red line*) and histologically verified probe location (*green line*). Black outline, brain; blue outline; dorsal striatum, purple outline; ventral striatum. Widefield-estimated probe locations closely match histologically verified probe locations. **b**, Widefield-estimated probe location of all trained mice plotted in Allen CCF coordinates. **c**, Example histology showing GCaMP6s fluorescence (*green*) and dye from the probe (*red*). **d**, Example multiunit correlation matrix by location along the probe for multiple sessions in the mouse from (c), with the borders of the striatum approximated medially by the lack of spikes in the ventricle and laterally by the sudden drop in local multiunit correlation. Dye from (c) corresponds to session 1 in (d) and histology-validated regions are labelled.

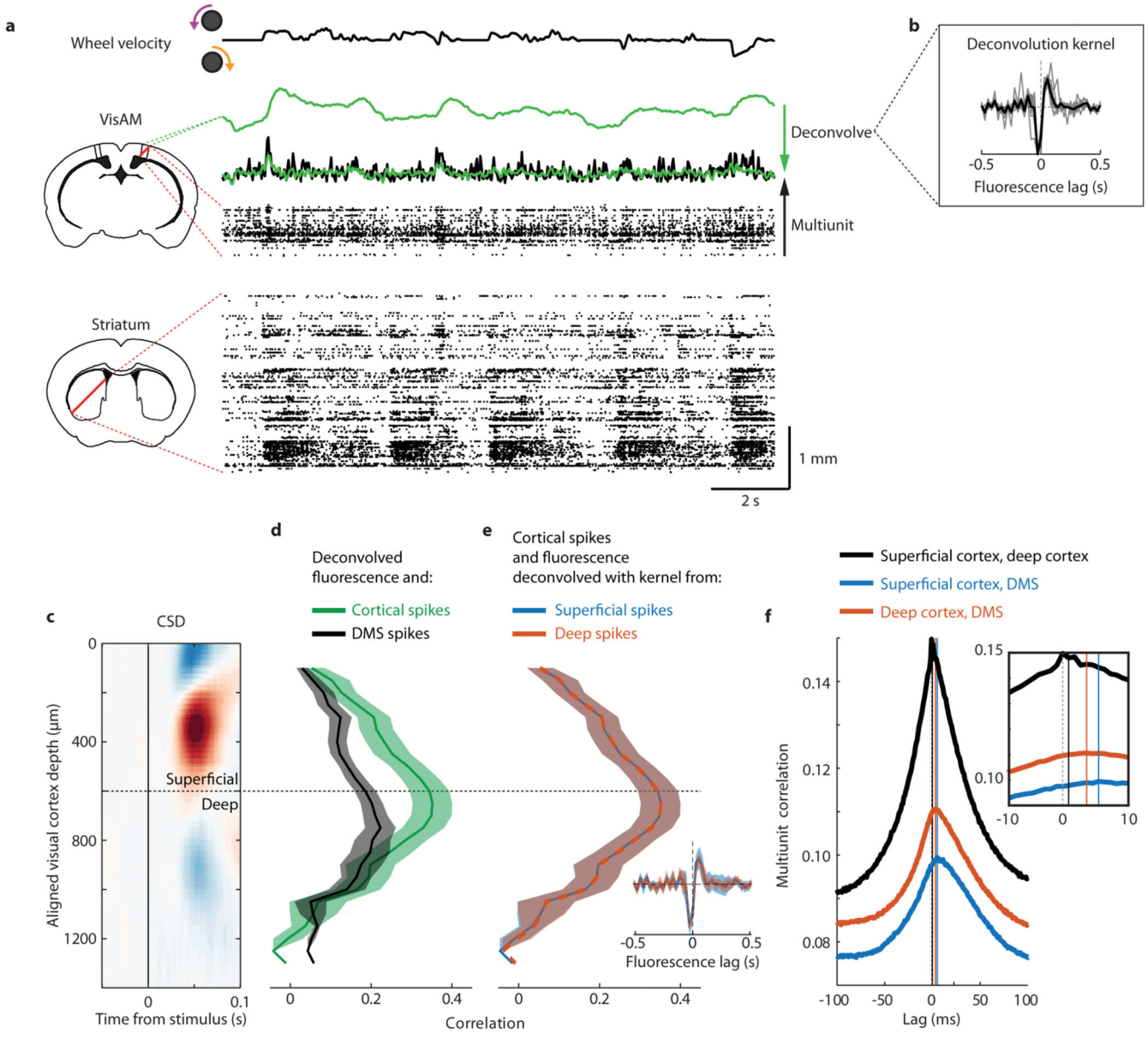

Europe PMC Funders Author Manuscripts

Extended Data Fig. 4. Relationship of cortical spiking with cortical fluorescence and with striatal spiking.

a, Example triple recording with widefield imaging, VISam electrophysiology, and striatal electrophysiology during the task. **b**, Deconvolution kernel obtained by predicting cortical multiunit spikes from cortical fluorescence around the probe (black, mean; grey, individual sessions). **c**, Current source density (CSD) from average stimulus responses aligned and averaged across sessions, used to identify superficial and deep cortical layers. Horizontal dashed line represents the estimated border between superficial and deep layers. **d**, Correlation of VISam spiking with deconvolved fluorescence (*green*) and DMS spiking (*black*) (mean ± s.e. across sessions). Cortical fluorescence and striatal spiking are both correlated to cortical spiking along a similar depth profile (correlation between fluorescence and striatal depth profiles compared to depth-shifted distribution, r = 0.57 ± 0.14 mean ± s.e. across 10 sessions, $p = 9.0*10^{-4}$). **e**, Correlation of VISam spiking with fluorescence deconvolved with a kernel created only using superficial spikes (*blue*) or deep spikes (*orange*) (mean ± s.e. across sessions). Inset: deconvolution kernels as in (b) created using only superficial or deep spikes. Kernels created from superficial or deep spikes are not different (2-way ANOVA on time and depth, depth p = 1 across 10 sessions) and correlation between spikes and deconvolved fluorescence does not depend on kernel (2way ANOVA on depth and kernel, kernel p = 0.97), indicating the deconvolution kernel is related to GcaMP6s dynamics consistently across depths. **f**, Cross-correlation of multiunit activity across superficial cortex, deep cortex, and DMS. Inset: zoomed-in plot. Deep cortical spiking leads striatal spiking by ~3ms (*orange vertical line*).

Europe PMC Funders Author Manuscripts

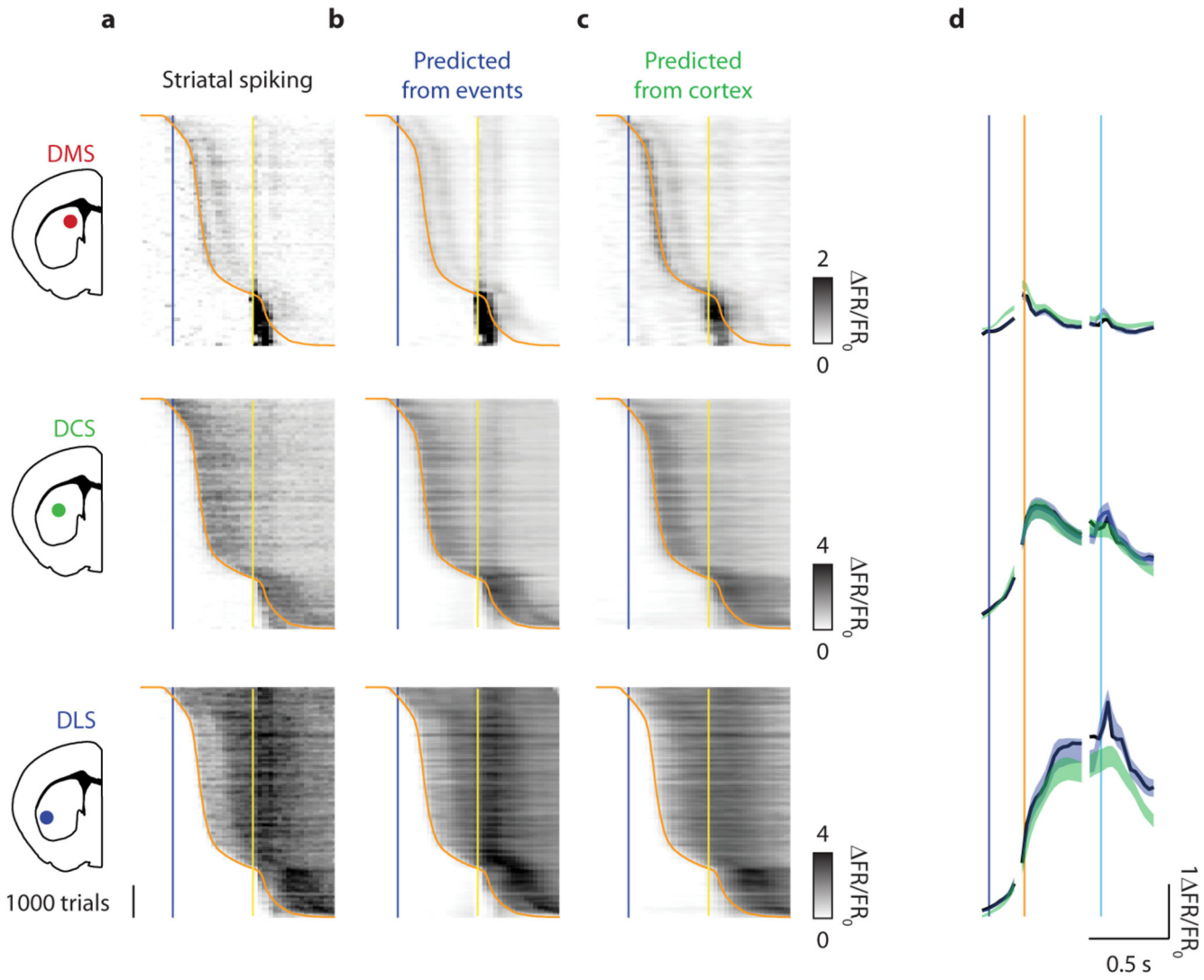

Extended Data Fig. 5. Striatal activity during trials with ipsilateral stimuli and ipsilaterally-orienting movements.

a, Activity for each striatal domain across all trials from all sessions with ipsilateral stimuli, ipsilaterally-orienting movements, and rewards, formatted as in Fig. 3a. Trials are sorted vertically by reaction time; blue line: stimulus onset, orange curve: movement onset, yellow line: Go cue. Activity within each timepoint is smoothed with a running average of 100 trials to display across-trial trends. **b**, Prediction of activity in each striatal domain by summing kernels for task events, formatted as in Fig. 3c. **c**, Prediction of striatal activity from cortical activity, formatted as in Fig. 3d. **d**, Trial-averaged activity in each striatal domain (*black*), predicted from task events (*blue*), and predicted from cortical activity (*green*), aligned to stimulus (*blue line*), movement (*orange line*), and reward (*cyan line*) (mean ± s.e. across sessions), formatted as in Fig. 3e.

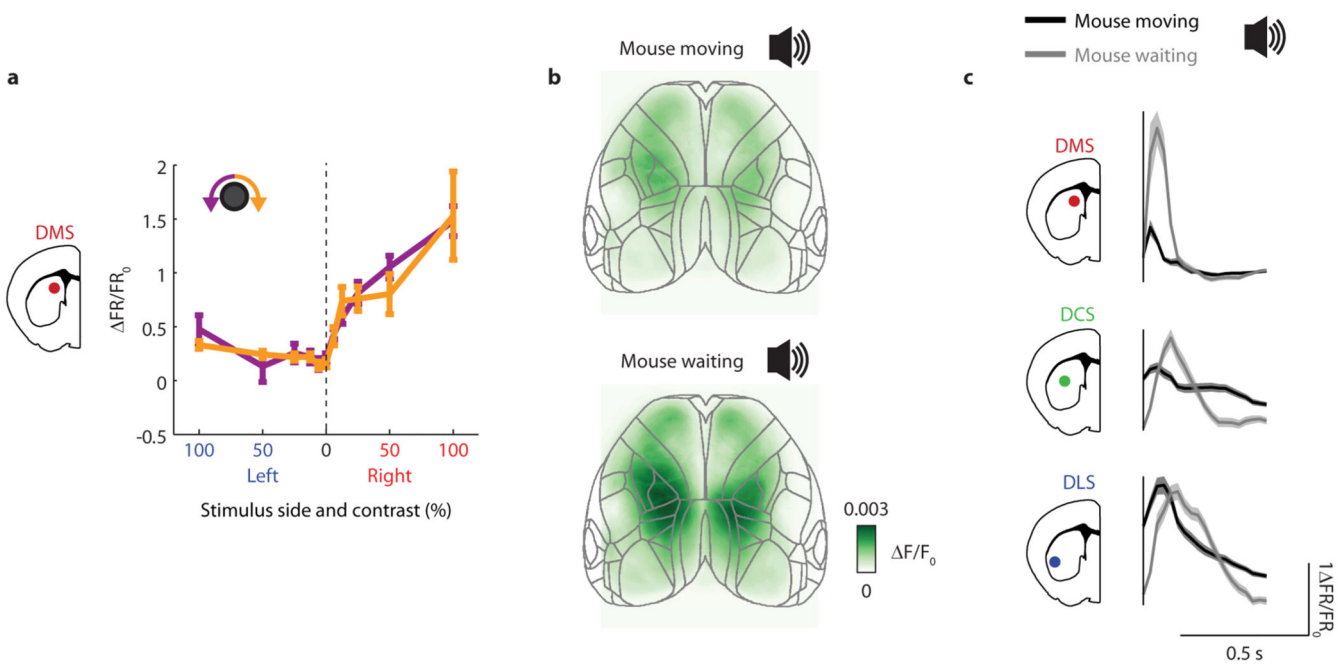

Extended Data Fig. 6. Visual responses in dorsomedial striatum do not depend on upcoming movement choice and responses to the auditory Go cue are suppressed by ongoing movement.

a, Curves show average stimulus response (0-0.2 s after stimulus onset) in DMS, as a function of contrast and side, for trials with < 500 ms reaction times and contralateral-orienting (purple) or ipsilateral-orienting (orange) movements (mean ± s.e. across sessions). Movement choice does not affect stimulus responses, indicating that stimulus responses are purely sensory, rather than linked to decisions (2-way ANOVA on stimulus and choice, interaction $p = 0.56$ for 77 sessions). **b**, Go cue kernel (lag = 50 ms after Go cue shown) obtained when fitting cortical activity from task events, for trials with movement onset before the Go cue (top) and after the Go cue (bottom). **c**, Go cue kernel obtained when fitting activity in each striatal domain from task events as in Fig. 3b, for trials with movement onset before the Go cue (*black*) and after the Go cue (*grey*). Note that responses to the Go cue are much larger in parietal cortex and DMS when the mouse is not moving.

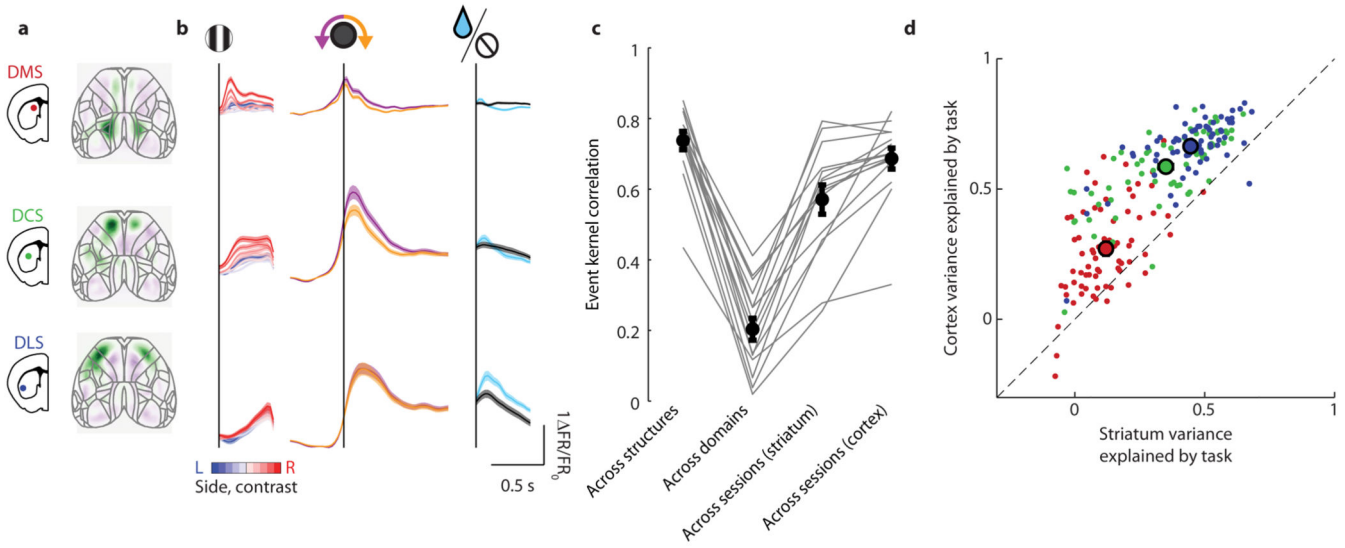

Extended Data Fig. 7. Task kernels for cortical activity associated with each striatal domain match task kernels for striatal activity.

a, Cortical maps used to define cortical activity associated with each striatal domain (from Fig. 2f, producing activity in Fig. 3d). **b**, Temporal kernels obtained when fitting cortical activity from task events for stimuli (left), movements (middle), and outcome (right) (mean ± s.e. across sessions), formatted as in Fig. 3b. **c**, Correlation of task kernels for striatal and cortical activity. Columns from left to right: correlation of associated striatal and cortical kernels, within the same session; correlation of striatal kernels for different domains within the same session; correlation of striatal kernels from different sessions but the same striatal domain, and correlation of cortical kernels obtained from different sessions, but associated with the same striatal domain. Grey lines show single sessions; black points and error bars show mean ± s.e. across mice. The kernels obtained for associated striatal domains and cortical regions are more correlated than kernels for different striatal domains (signed-rank test, $p = 6.1*10^{-5}$ for 15 mice), indicating task kernels are domain-specific and shared between associated cortical and striatal regions. Correlations are also higher between associated striatal and cortical activity within-sessions, than between kernels fit to the same striatal domain on different sessions (signed-rank test, $p = 1.2*10^{-4}$), indicating that differences between cortical and striatal task responses are smaller than session-to-session variability. **d**, Cross-validated fraction of variance explained by task events for striatal activity vs. associated cortical activity. Small dots, sessions; large dots, mean ± s.e. across sessions; colour, striatal domain. Explained variance from task events is correlated between the cortex and striatum (correlation, $r = 0.68$ $p = 1.14*10^{-10}$ across 77 sessions).

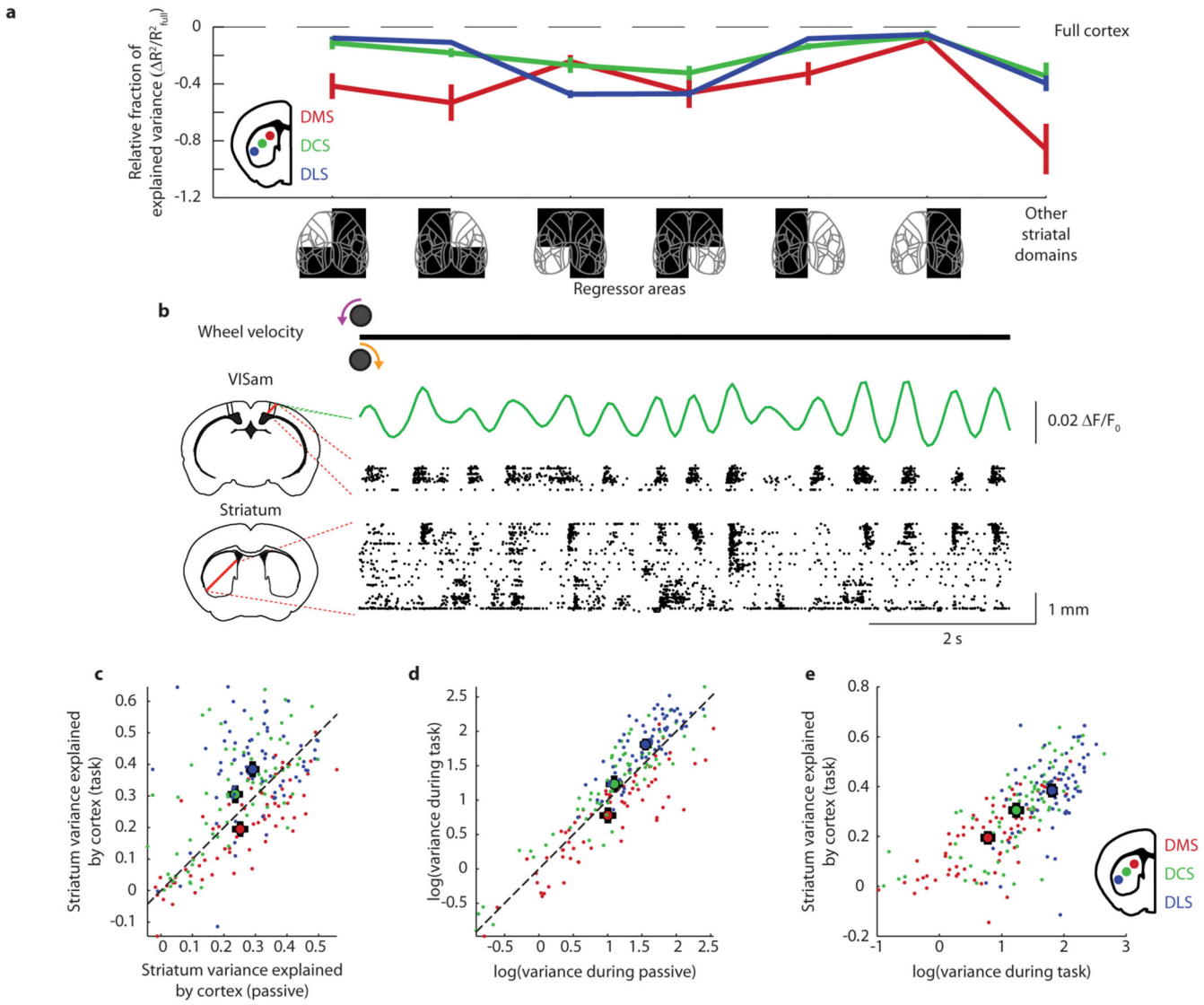

Extended Data Fig. 8. Prediction of striatal activity from subregions of cortex, from other striatal domains, and from the cortex during passive periods.

a, Activity in each striatal domain predicted from subregions of cortex (indicated by white regions in diagrams below x-axis) or from the other two striatal domains (far right). Each curve shows the relative cross-validated fraction of explained variance ((R^2region - R^2full cortex) /R^2full cortex) for the color-coded striatal domain (mean ± s.e. across sessions). Predictions are best from the associated cortical regions (2-way ANOVA on session and cortical subregion, subregion DMS $p = 4.6*10^{-3}$, DCS $p = 4.8*10^{-5}$, DLS $p = 3.1*10^{-85}$ across 77 sessions) and striatal activity is less well predicted from other striatal domains than from cortex (signed-rank test, DMS $p = 1.6*10^{-10}$, DCS $p = 2.1*10^{-5}$, DLS $p = 8.4*10^{-10}$ across 77 sessions). **b**, Example wheel trace, deconvolved cortical fluorescence, visual cortical electrophysiology, and striatal electrophysiology session in the passive context (viewing visual noise stimuli), showing coherent low-frequency oscillations in VISam and DMS (formatted as in Extended Data Fig. 4a, from the same session session). **c**, Cross-

validated fraction of striatal variance explained from cortex in task vs. passive contexts. Small dots, sessions; large dots, mean ± s.e. across sessions; colour, striatal domain. DMS is predicted slightly better from cortex in the passive state, but DCS and DLS are predicted slightly worse the passive state (signed-rank test, DMS $p = 6.2*10^{-7}$, DCS $p = 1.9*10^{-4}$, DLS $p = 1.6*10^{-5}$ across 77 sessions). **d**, Variance of striatal activity across task and passive states, legend as in (b). During the passive state, DMS exhibits more variance while DCS and DLS exhibit less variance (signed-rank test, DMS $p = 3.0*10^{-6}$, DCS $p = 1.3*10^{-4}$, DLS $p = 1.1*10^{-10}$ across 77 sessions), matching the differences in predictability between states. **e**, Cross-validated fraction of striatal explained variance from the cortex vs. variance of striatal activity during task performance, legend as in (b). Cortex-explained variance is consistently related to activity variance across domains (ANCOVA, domain $p = 0.22$, domain-activity variance interaction $p = 0.76$).

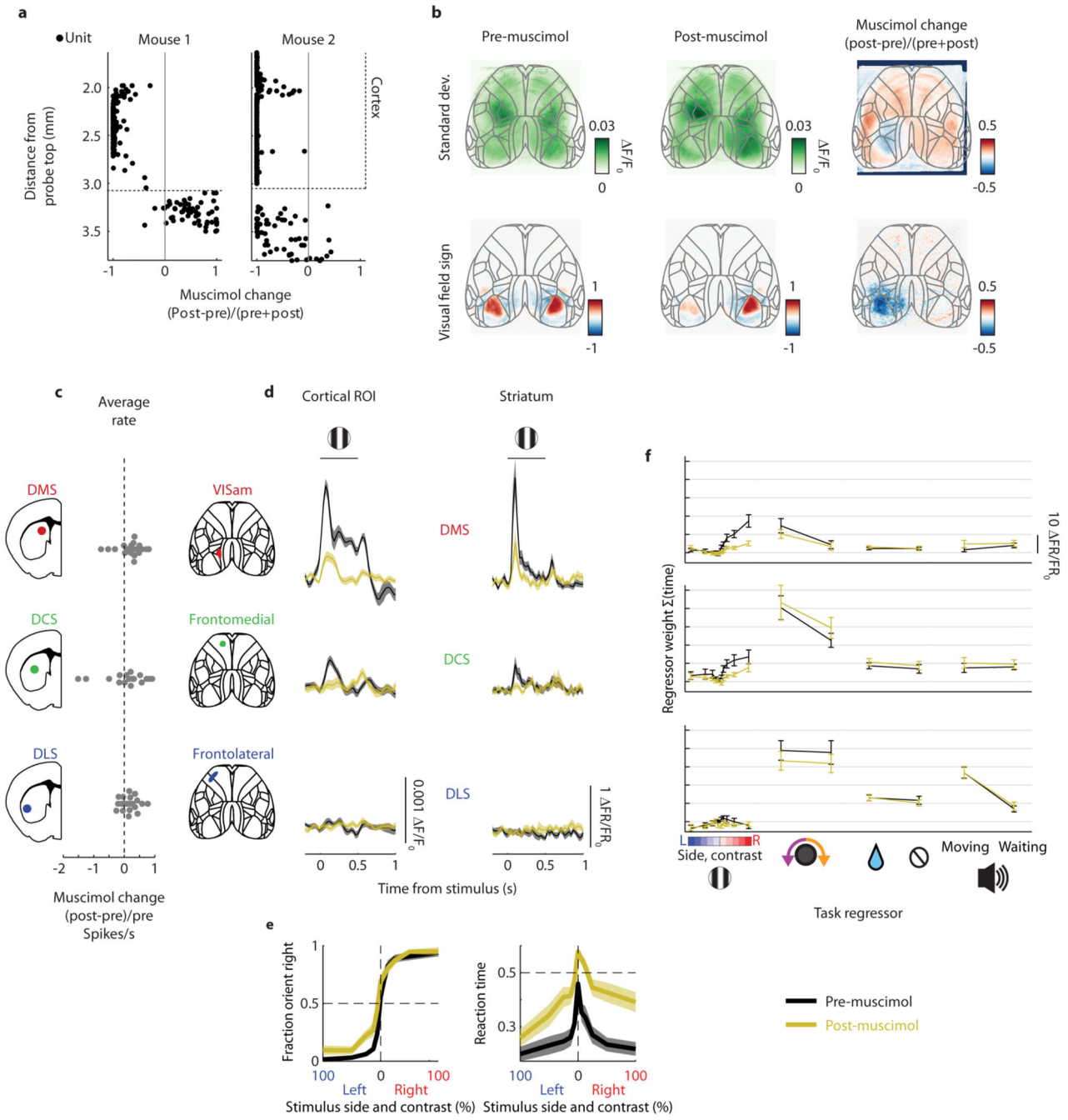

Extended Data Fig. 9. Visual cortical inactivation selectively eliminates striatal visual responses.
a, Cortical unit firing rate change across topical muscimol application. Horizontal dotted line indicates bottom edge of cortex. Topical muscimol effectively silences the full cortical depth. **b**, Deconvolved cortical fluorescence standard deviation (top) and retinotopic visual field sign (bottom) before and after muscimol application. Muscimol was centred on VISam and spread laterally to other visual areas. **c**, Relative firing rate change in each striatal domain before and after cortical inactivation (dots are sessions). Firing rate increases slightly after cortical inactivation (signed-rank test, DMS p = 0.04, DCS p = 0.02, DLS

p = 0.02 across 22 sessions). **d**, Passive responses to visual stimuli in cortical ROIs (left) and corresponding striatal domains (right) before (*black*) and after (*yellow*) inactivation of visual cortex. Muscimol reduced the stimulus response in VISam and DMS proportionally within each session (correlation between fractional reduction of each area: r = 0.48, p = 0.04 across 22 sessions). **e**, Psychometric curve (left) and median reaction (right) as a function of stimulus contrast and side as in Extended Data Fig. 1b, before (*black*) and after (*yellow*) muscimol in visual cortex (mean ± s.e. across sessions). Task performance becomes worse asymmetrically across stimuli (2-way ANOVA on stimulus and condition, interaction p = 0.04 across 22 sessions) and reaction times become longer across stimuli (2-way ANOVA on stimulus and condition, condition $p = 1.1*10^{-26}$ across 22 sessions). **f**, Kernels using task events to predict striatal activity before (*black*) and after (*yellow*) visual cortical muscimol (mean ± s.e. across sessions). Stimulus kernel weights decrease after muscimol while other kernel weights do not change significantly (2-way ANOVA on regressor and condition, condition effect on stimuli regressors DMS $p = 2.0*10^{-7}$, DCS $p = 8.4*10^{-6}$, DLS p = 0.03, p > 0.05 for other domains and regressors across 22 sessions).

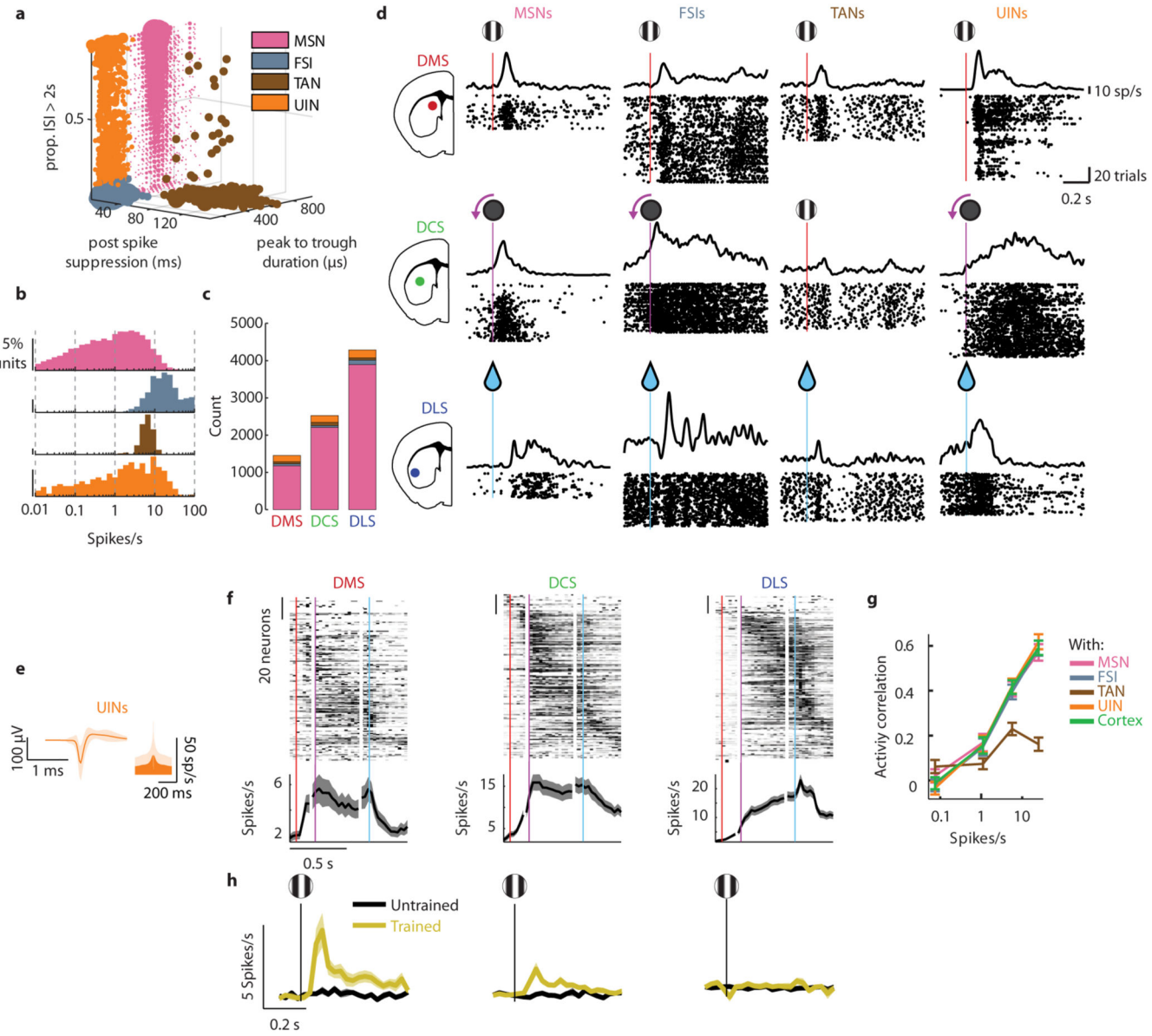

Extended Data Fig. 10. Identifying striatal cell types with electrophysiology, and unidentified interneuron (UIN) activity.

a, Electrophysiological properties used to classify striatal cell types. Striatal cells were identified as medium spiny neurons (MSNs), fast-spiking interneurons (FSIs), tonically-active neurons (TANs) and a fourth class of unidentified interneurons (UINs), according to waveform duration, length of post-spike suppression, and fraction of long inter-spike intervals. **b**, Histogram of firing rates across all units within each cell type. **c**, Number of units in each striatal domain classified as each cell type. **d**, Averaged and smoothed firing rates (lines) and raster plots across trials (dots) for one example cell of each type in each domain, aligned to the indicated task event. Top row: DMS; middle row, DCS; bottom row, DLS. **e**, Waveform and autocorrelogram of unidentified interneurons (UINs) (mean ± s.d. across cells). **f**, Heatmaps, spiking in individual cells aligned to contralateral stimuli (left),

Europe PMC Funders Author Manuscripts

contralaterally-orienting movements (middle), and rewards (right), averaged across trials with reaction times less than 500 ms, max-normalized, and sorted by time of maximum activity using half of the trials and plotting the other half of trials, formatted as in Fig. 4b. Line plots, average activity across neurons, formatted as in Fig. 4c. **g**, Correlation of the activity of each neuron (rows within heatmaps of c) with the average activity within cell types or cortical activity from an ROI corresponding to each domain, calculated from non-overlapping sessions to account for interneuron sparsity (mean ± s.e. across sessions), formatted as in Fig. 4d. UINs were equally correlated to other UINs, MSNs, FSIs, and cortical activity (2-way ANOVA on firing rate and type, type $p = 0.56$ across 77 sessions) and uncorrelated to TAN activity (2-way ANOVA on firing rate and type, type $p = 2.7*10^{-12}$ across 77 sessions). **h**, Activity during passive stimulus presentations in untrained (*black*) and trained (*yellow*) mice (mean ± s.e. across sessions), activity increases in DMS and DCS (time window 0-0.2 s, rank-sum test, DMS: $p = 5.5*10^{-4}$, DCS: $p = 1.4*10^{-4}$ across 77 sessions).

Acknowledgements

We thank Charu Reddy, Miles Wells, Laura Funnell, and Hamish Forrest for mouse husbandry and training, Rakesh Raghupathy, Izzie Prankerd, and David Orme for histology, Dana Cohen for helpful discussions, and the NVIDIA Corporation for donation of a Titan X GPU. This work was supported by a Newton International Fellowship, EMBO Fellowship (ALTF 1428-2015), and a Human Frontier Science Program Fellowship (LT226/2016-L) to A.J.P, a Wellcome Trust PhD Studentship to JMJF, a Human Frontier Science Program Fellowship (LT001071/2015-L) and Marie Skłodowska-Curie fellowship of the E.U. Horizon 2020 (656528) to N.A.S., Wellcome Trust grants 205093, 204915 to K.DH. and M.C, ERC grant 694401 to K.D.H, M.C. holds the GlaxoSmithKline / Fight for Sight Chair in Visual Neuroscience.

Data availability

The datasets generated during the current study are available as downloadable files at https://osf.io/x4q26/.

Code availability

The code used to analyze the data are available at https://github.com/petersaj/Peters_et_al_Nature_2020.

References

1. Hintiryan H, Foster NN, Bowman I, Bay M, Song MY, Gou L, Yamashita S, Bienkowski MS, Zingg B, Zhu M, Yang XW, et al. The mouse cortico-striatal projectome. Nat Neurosci. 2016; 19: 1100–1114. [PubMed: 27322419]
2. Hunnicutt BJ, Jongbloets BC, Birdsong WT, Gertz KJ, Zhong H, Mao T. A comprehensive excitatory input map of the striatum reveals novel functional organization. Elife. 2016; 5: 1–32.
3. Friedman A, Homma D, Gibb LGG, Amemori K, Rubin SJJ, Hood ASS, Riad MHH, Graybiel AMM. A Corticostriatal Path Targeting Striosomes Controls Decision-Making under Conflict. Cell. 2015; 161: 1320–1333. [PubMed: 26027737]
4. Gremel CM, Chancey JH, Atwood BK, Luo G, Neve R, Ramakrishnan C, Deisseroth K, Lovinger DM, Costa RM. Endocannabinoid Modulation of Orbitostriatal Circuits Gates Habit Formation. Neuron. 2016; 90: 1312–1324. [PubMed: 27238866]
5. Znamenskiy P, Zador AM. Corticostriatal neurons in auditory cortex drive decisions during auditory discrimination. Nature. 2013; 497: 482–5. [PubMed: 23636333]

6. Fujii N, Graybiel AM. Time-varying covariance of neural activities recorded in striatum and frontal cortex as monkeys perform sequential-saccade tasks. Proc Natl Acad Sci. 2005; 102: 9032–9037. [PubMed: 15956185]
7. Martiros N, Burgess AA, Graybiel AM. Inversely Active Striatal Projection Neurons and Interneurons Selectively Delimit Useful Behavioral Sequences. Curr Biol. 2018; 0: 1–14.
8. Buch ER, Brasted PJ, Wise SP. Comparison of population activity in the dorsal premotor cortex and putamen during the learning of arbitrary visuomotor mappings. Exp brain Res. 2006; 169: 69–84. [PubMed: 16284756]
9. Pidoux M, Mahon S, Deniau JM, Charpier S. Integration and propagation of somatosensory responses in the corticostriatal pathway: An intracellular study in vivo. J Physiol. 2011; 589: 263–281. [PubMed: 21059765]
10. Kim HF, Hikosaka O. Distinct Basal Ganglia Circuits Controlling Behaviors Guided by Flexible and Stable Values. Neuron. 2013; 79: 1001–1010. [PubMed: 23954031]
11. Wang L, Rangarajan KV, Gerfen CR, Krauzlis RJ. Activation of Striatal Neurons Causes a Perceptual Decision Bias during Visual Change Detection in Mice. Neuron. 2018; 97: 1369–1381. e5 [PubMed: 29503185]
12. Guo L, Walker WI, Ponvert ND, Penix PL, Jaramillo S. Stable representation of sounds in the posterior striatum during flexible auditory decisions. Nat Commun. 2018; 9 1534 [PubMed: 29670112]
13. Rueda-Orozco PE, Robbe D. The striatum multiplexes contextual and kinematic information to constrain motor habits execution. Nat Neurosci. 2015; 18: 453–460. [PubMed: 25622144]
14. Tai L-H, Lee AM, Benavidez N, Bonci A, Wilbrecht L. Transient stimulation of distinct subpopulations of striatal neurons mimics changes in action value. Nat Neurosci. 2012; 15: 1281–9. [PubMed: 22902719]
15. Yartsev MM, Hanks TD, Yoon AM, Brody CD. Causal contribution and dynamical encoding in the striatum during evidence accumulation. Elife. 2018; 7 245316
16. Kincaid AE, Zheng T, Wilson CJ. Connectivity and convergence of single corticostriatal axons. J Neurosci. 1998; 18: 4722–4731. [PubMed: 9614246]
17. Huerta-Ocampo I, Mena-Segovia J, Bolam JP. Convergence of cortical and thalamic input to direct and indirect pathway medium spiny neurons in the striatum. Brain Struct Funct. 2014; 219: 1787–1800. [PubMed: 23832596]
18. Oh SW, Harris JA, Ng L, Winslow B, Cain N, Mihalas S, Wang Q, Lau C, Kuan L, Henry AM, Mortrud MT, et al. A mesoscale connectome of the mouse brain. Nature. 2014; 508: 207–14. [PubMed: 24695228]
19. Emmons EB, De Corte BJ, Kim Y, Parker KL, Matell MS, Narayanan NS. Rodent medial frontal control of temporal processing in the dorsomedial striatum. J Neurosci. 2017; 37: 1376–17.
20. Lemke SM, Ramanathan DS, Guo L, Won SJ, Ganguly K. Emergent modular neural control drives coordinated motor actions. Nat Neurosci. 2019; 22: 1122–1131. [PubMed: 31133689]
21. Apicella P. Tonically active neurons in the primate striatum and their role in the processing of information about motivationally relevant events. Eur J Neurosci. 2002; 16: 2017–2026. [PubMed: 12473069]
22. Gage GJ, Stoetzner CR, Wiltschko AB, Berke JD. Selective Activation of Striatal Fast-Spiking Interneurons during Choice Execution. Neuron. 2010; 67: 466–479. [PubMed: 20696383]
23. Stalnaker TA, Berg B, Aujla N, Schoenbaum G. Cholinergic Interneurons Use Orbitofrontal Input to Track Beliefs about Current State. J Neurosci. 2016; 36: 6242–57. [PubMed: 27277802]
24. Bolam JP, Hanley JJ, Booth PAC, Bevan MD. Synaptic organisation of the basal ganglia. J Anat. 2000; 196: 527–542. [PubMed: 10923985]
25. Kato S, Kuramochi M, Kobayashi K, Fukabori R, Okada K, Uchigashima M, Watanabe M, Tsutsui Y, Kobayashi K. Selective Neural Pathway Targeting Reveals Key Roles of Thalamostriatal Projection in the Control of Visual Discrimination. J Neurosci. 2011; 31: 17169–17179. [PubMed: 22114284]
26. Ponvert ND, Jaramillo S. Auditory Thalamostriatal and Corticostriatal Pathways Convey Complementary Information about Sound Features. J Neurosci. 2019; 39: 271–280. [PubMed: 30459227]

27. Burke DA, Rotstein HG, Alvarez VA. Striatal Local Circuitry: A New Framework for Lateral Inhibition. Neuron. 2017; 96: 267–284. [PubMed: 29024654]
28. Choi EY, Yeo BTT, Buckner RL. The organization of the human striatum estimated by intrinsic functional connectivity. J Neurophysiol. 2012; 108: 2242–2263. [PubMed: 22832566]
29. Burgess CP, Lak A, Steinmetz NA, Zatka-Haas P, Bai Reddy C, Jacobs EAK, Linden JF, Paton JJ, Ranson A, Schröder S, Soares S, et al. High-Yield Methods for Accurate Two-Alternative Visual Psychophysics in Head-Fixed Mice. Cell Rep. 2017; 20: 2513–2524. [PubMed: 28877482]
30. Wekselblatt JB, Flister ED, Piscopo DM, Niell CM. Large-scale imaging of cortical dynamics during sensory perception and behavior. J Neurophysiol. 2016; 115: 2852–2866. [PubMed: 26912600]
31. Jun JJ, Steinmetz NA, Siegle JH, Denman DJ, Bauza M, Barbarits B, Lee AK, Anastassiou CA, Andrei A, Aydin Ç, Barbic M, et al. Fully integrated silicon probes for high-density recording of neural activity. Nature. 2017; 551: 232–236. [PubMed: 29120427]
32. Allen WE, Kauvar IV, Chen MZ, Richman EB, Yang SJ, Chan K, Gradinaru V, Deverman BE, Luo L, Deisseroth K. Global Representations of Goal-Directed Behavior in Distinct Cell Types of Mouse Neocortex. Neuron. 2017; 94: 891–907. e6 [PubMed: 28521139]
33. Shepherd GMG. Corticostriatal connectivity and its role in disease. Nat Rev Neurosci. 2013; 14: 278–291. [PubMed: 23511908]
34. Senzai Y, Fernandez-Ruiz A, Buzsáki G. Layer-Specific Physiological Features and Interlaminar Interactions in the Primary Visual Cortex of the Mouse. Neuron. 2019; 101: 500–513. e5 [PubMed: 30635232]
35. Mallet N, Le Moine C, Charpier S, Gonon F. Feedforward inhibition of projection neurons by fast-spiking GABA interneurons in the rat striatum in vivo. J Neurosci. 2005; 25: 3857–3869. [PubMed: 15829638]
36. Inokawa H, Yamada H, Matsumoto N, Muranishi M, Kimura M. Juxtacellular labeling of tonically active neurons and phasically active neurons in the rat striatum. Neuroscience. 2010; 168: 395–404. [PubMed: 20371269]
37. Yamin HG, Stern EA, Cohen D. Parallel processing of environmental recognition and locomotion in the mouse striatum. J Neurosci. 2013; 33: 473–84. [PubMed: 23303928]
38. Schmitzer-Torbert NC, Redish AD. Task-dependent encoding of space and events by striatal neurons is dependent on neural subtype. Neuroscience. 2008; 153: 349–360. [PubMed: 18406064]
39. Kim N, Li HE, Hughes RN, Watson GDR, Gallegos D, West AE, Kim IH, Yin HH. A striatal interneuron circuit for continuous target pursuit. Nat Commun. 2019; 10 2715 [PubMed: 31222009]
40. Benhamou L, Kehat O, Cohen D. Firing pattern characteristics of tonically active neurons in rat striatum: context dependent or species divergent? J Neurosci. 2014; 34: 2299–304. [PubMed: 24501368]
41. Marche K, Martel A-C, Apicella P. Differences between Dorsal and Ventral Striatum in the Sensitivity of Tonically Active Neurons to Rewarding Events. Front Syst Neurosci. 2017; 11: 1–12. [PubMed: 28154528]
42. Johansson Y, Silberberg G. The Functional Organization of Cortical and Thalamic Inputs onto Five Types of Striatal Neurons Is Determined by Source and Target Cell Identities. Cell Rep. 2020; 30: 1178–1194. e3 [PubMed: 31995757]
43. Orsolic I, Rio M, Mrsic-Flogel TD, Znamenskiy P. Mesoscale cortical dynamics reflect the interaction of sensory evidence and temporal expectation during perceptual decision-making. bioRxiv. 2019; 552026 doi: 10.1101/552026
44. Sales-Carbonell C, Taouali W, Khalki L, Pasquet MO, Petit LF, Moreau T, Rueda-Orozco PE, Robbe D. No Discrete Start/Stop Signals in the Dorsal Striatum of Mice Performing a Learned Action. Curr Biol. 2018; 1–12. DOI: 10.1016/j.cub.2018.07.038
45. Rothwell PE, Hayton SJ, Sun GL, Fuccillo MV, Lim BK, Malenka RC. Input-and Output-Specific Regulation of Serial Order Performance by Corticostriatal Circuits. Neuron. 2015; 88: 345–356. [PubMed: 26494279]

46. O'Hare JK, Ade KK, Sukharnikova T, Van Hooser SD, Palmeri ML, Yin HH, Calakos N. Pathway-Specific Striatal Substrates for Habitual Behavior. Neuron. 2016; 89: 472–479. [PubMed: 26804995]
47. Xiong Q, Znamenskiy P, Zador AM. Selective corticostriatal plasticity during acquisition of an auditory discrimination task. Nature. 2015; 521: 348–351. [PubMed: 25731173]
48. Koralek AC, Costa RM, Carmena JM. Temporally precise cell-specific coherence develops in corticostriatal networks during learning. Neuron. 2013; 79: 865–72. [PubMed: 23954030]
49. Owen SF, Berke JD, Kreitzer AC. Fast-Spiking Interneurons Supply Feedforward Control of Bursting, Calcium, and Plasticity for Efficient Learning. Cell. 2018; 172: 683–695. e15 [PubMed: 29425490]
50. Steinmetz NA, Buetfering C, Lecoq J, Lee CR, Peters AJ, Jacobs EAK, Coen P, Ollerenshaw DR, Valley MT, de Vries SEJ, Garrett M, et al. Aberrant Cortical Activity in Multiple GCaMP6-Expressing Transgenic Mouse Lines. Eneuro. 2017; 4 ENEURO.0207-17.2017
51. Bhagat J, Wells MJ, Harris KD, Carandini M, Burgess CP. Rigbox: An open-source toolbox for probing neurons and behavior. eNeuro. 2020; 7: 1–12.
52. Wang Q, Ding SL, Li Y, Royall J, Feng D, Lesnar P, Graddis N, Naeemi M, Facer B, Ho A, Dolbeare T, et al. The Allen Mouse Brain Common Coordinate Framework: A 3D Reference Atlas. Cell. 2020; 181: 936–953. e20 [PubMed: 32386544]
53. Zhuang J, Ng L, Williams D, Valley M, Li Y, Garrett M, Waters J. An extended retinotopic map of mouse cortex. Elife. 2017; 6: 1–29.
54. Rossant C, Kadir SN, Goodman DFM, Schulman J, Hunter MLD, Saleem AB, Grosmark A, Belluscio M, Denfield GH, Ecker AS, Tolias AS, et al. Spike sorting for large, dense electrode arrays. Nat Neurosci. 2016; 19: 634–641. [PubMed: 26974951]
55. Siegle JH, López AC, Patel YA, Abramov K, Ohayon S, Voigts J, Black C, Voigts J, Buccino AP, Elle M, Ciliberti D, et al. Open Ephys: An open-source, plugin-based platform for multichannel electrophysiology. J Neural Eng. 2017; 14
56. Deligkaris K, Bullmann T, Frey U. Extracellularly recorded somatic and neuritic signal shapes and classification algorithms for high-density microelectrode array electrophysiology. Front Neurosci. 2016; 10: 1–11. [PubMed: 26858586]
57. Hill DN, Mehta SB, Kleinfeld D. Quality metrics to accompany spike sorting of extracellular signals. J Neurosci. 2011; 31: 8699–8705. [PubMed: 21677152]

Europe PMC Funders Author Manuscripts

Europe PMC Funders Author Manuscripts

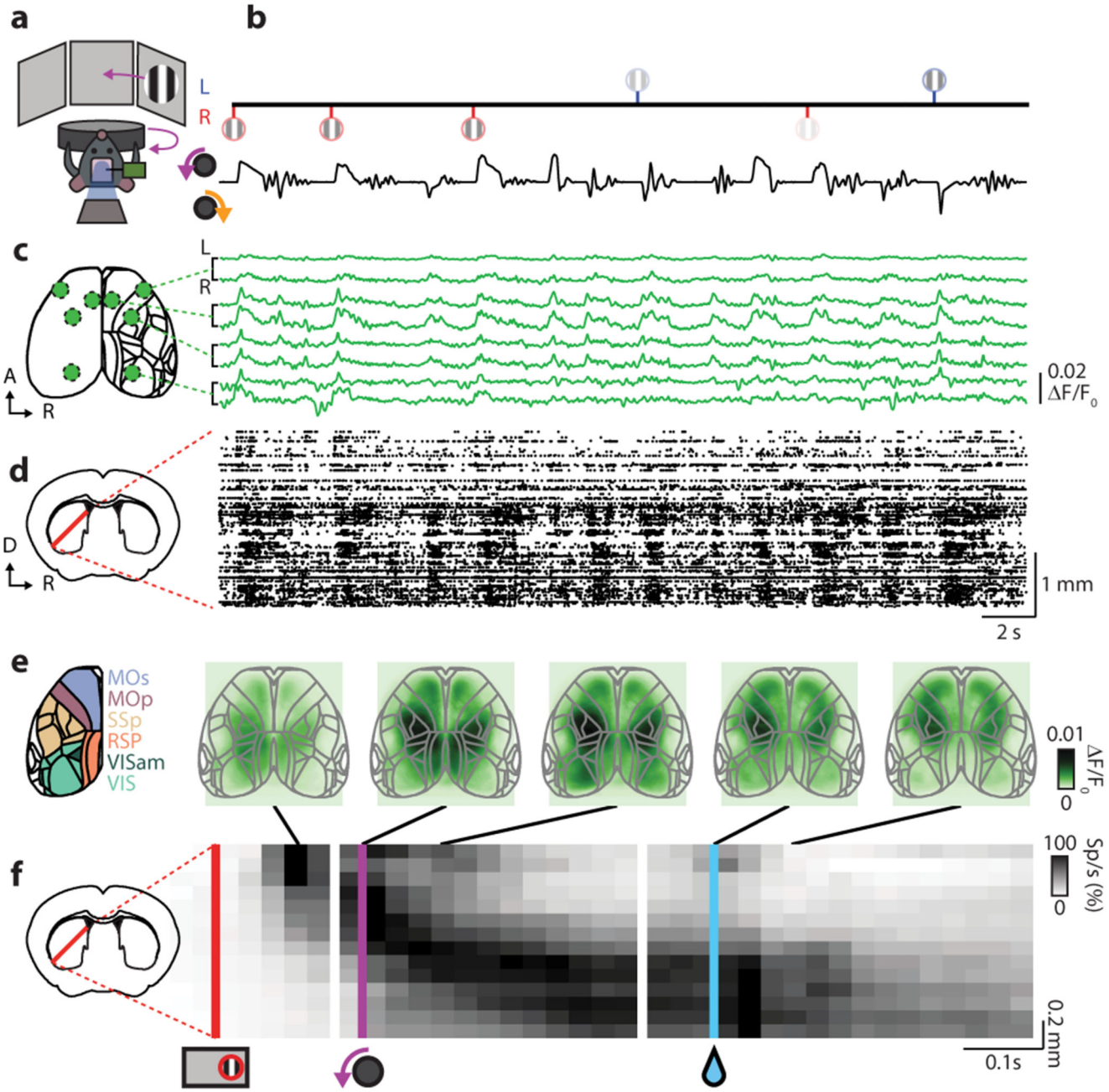

Figure 1. Cortex and striatum show spatial gradients of sensorimotor activity during visually guided behaviour.

a, Cartoon of the task, showing a mouse turning a steering wheel surrounded by three screens. **b**, Timeline of task events from an example session, showing gratings of various contrasts appearing on the left or right of the animal (*top*) and velocity of the steering wheel (*bottom*). **c**, Cortical activity measured by widefield calcium imaging during the period in (b). Deconvolved fluorescence traces are shown for orofacial and limb primary motor cortex (MOp), secondary motor cortex (MOs), and primary visual cortex (VISp). **d**, Spikes measured simultaneously across the dorsal striatum during the same period. **e**, Deconvolved

cortical fluorescence maps, at five timepoints averaged across all trials of all sessions with right-hand stimuli, correct counter-clockwise wheel turns, and reaction times < 500 ms. MOp and MOs: primary and secondary motor cortex; SSp: Primary somatosensory cortex; VIS: visual cortex; RSP: retrosplenial cortex. **f**, Mean multiunit firing rate in striatum as a function of location and time, averaged over the same events as in (e). The three grayscale panels represent activity aligned to visual stimulus onset (*red line*); contralaterally-orienting movements (*purple line*), and reward delivery (*cyan line*). Firing rates are arranged by distance from the lateral striatal border, averaged across sessions, and max-normalized.

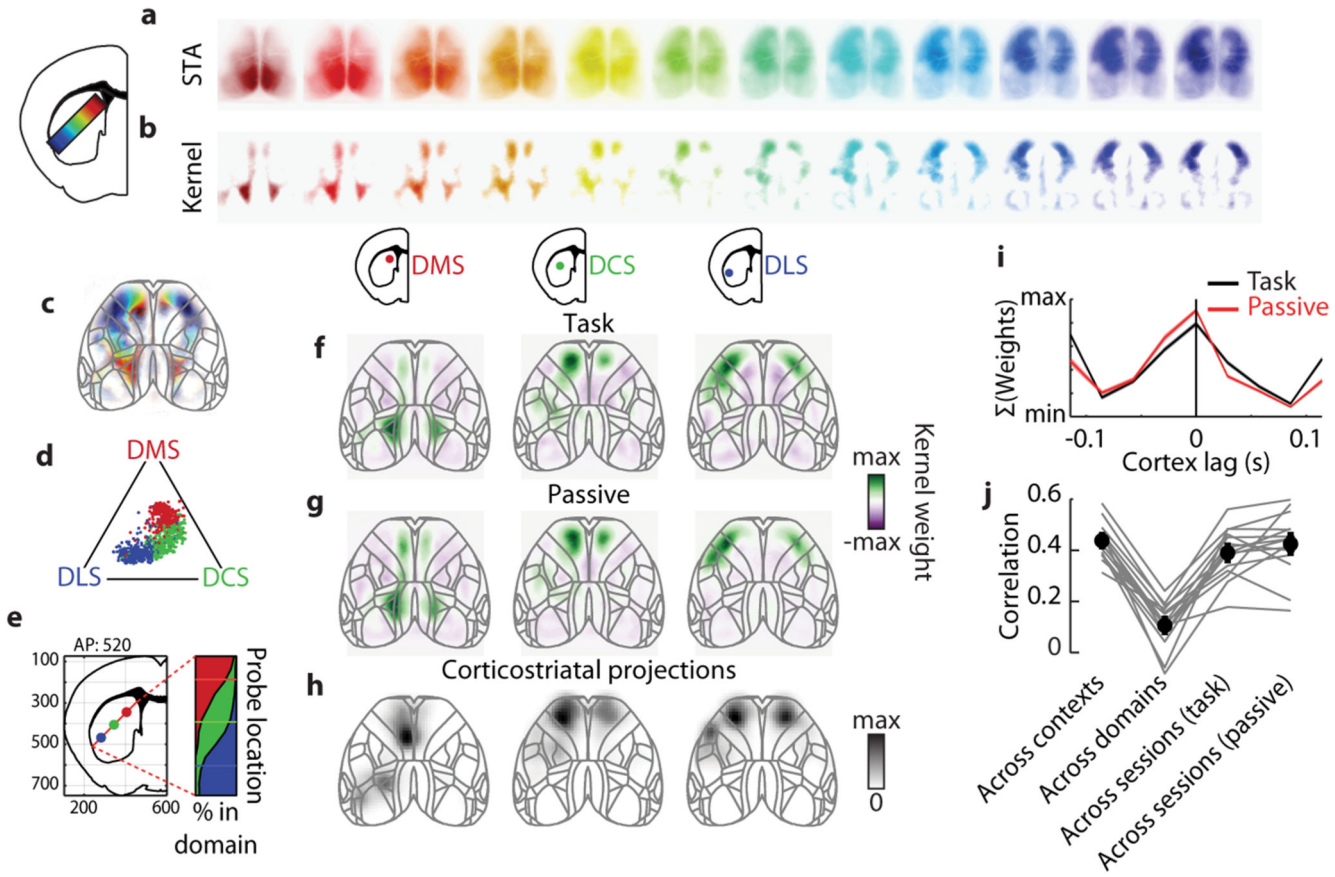

Figure 2. Striatal domains are topographically correlated with connected cortical regions.

a, Spike-triggered average of deconvolved cortical fluorescence for multiunit activity at each striatal location (indexed by colours), averaged across sessions from all mice. **b**, Regressed spatial kernels corresponding to locations in (a). **c**, Centre-of-mass of the kernel weights in (b), using the same colour scale as (a). **d**, Ternary plot showing relative correlation of the cortical kernels for each 200 μm striatal segment in each session (*dots*) with the three template kernels used to assign each segment to a striatal domain (*vertices*). **e**, Left, centre-of-mass CCF location for each striatal domain estimated from all striatal segments in (d); right, cumulative fraction of striatal segments in (d) categorized into each domain relative to CCF location. **f**, Mean cortical spatial kernels for each striatal domain (lag = 0 s) during the task, averaged across sessions and max-normalized. **g**, Cortical spatial kernels as in (f) computed while mice passively viewed visual noise stimuli. **h**, Density of cortical locations projecting to each striatal domain, data from the Allen Mouse Brain Connectivity Atlas [18] . **i**, Time course of spatially summed cortical kernels weights, measured in the behavioural task (*black*) or during passive viewing of visual noise (*red*). Curves show mean across domains and sessions ± s.e. across sessions. The kernel weights are larger for the cortex leading striatum (signed-rank test, $p = 2.5*10^{-6}$ across 77 sessions). **j**, Correlation of spatiotemporal cortical kernels across contexts (task vs. passive), across striatal domains, and across sessions (mean ± s.e. across mice). Cortical kernels fit from different domains

Europe PMC Funders Author Manuscripts

are significantly less correlated than kernels from different behavioural contexts or recording sessions (signed-rank test, $p = 6.1*10^{-5}$ across 15 mice).

Europe PMC Funders Author Manuscripts

Europe PMC Funders Author Manuscripts

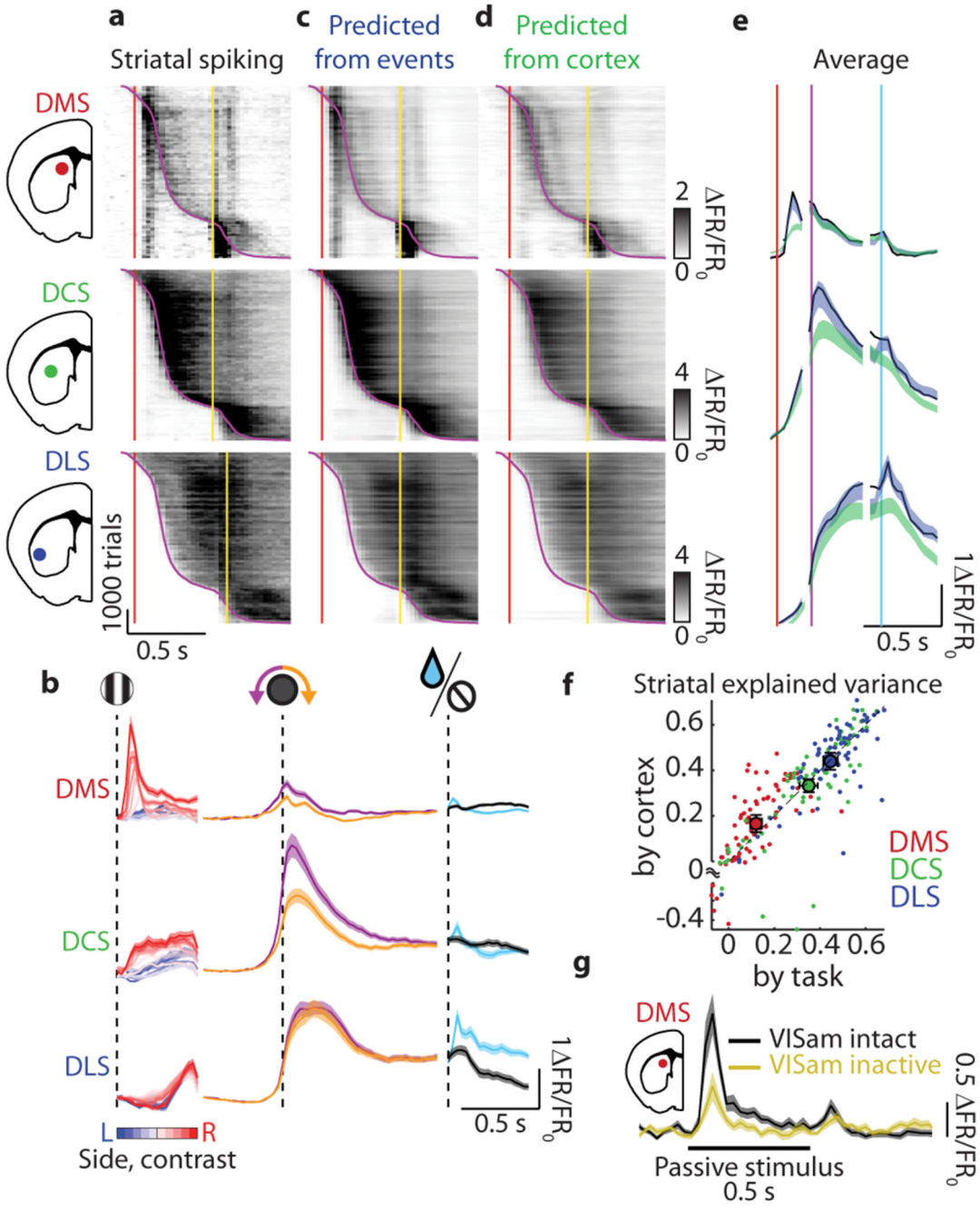

Figure 3. Striatal sensorimotor activity reflects associated cortical activity.

a, Multiunit activity in each striatal domain, shown for all trials with contralateral stimuli, contralaterally-orienting movements, and rewards. Trials are aligned by stimulus onset (*red line*), which was followed 500 ms later by a Go cue (*yellow line*). Trials are combined across sessions and sorted by reaction time (time of movement onset, *purple curve*). For graphical purposes, activity at each time is smoothed with a running average of 100 trials to highlight features that are consistent across trials. **b**, Event kernels predicting activity in each striatal domain from task events. Left column: kernels for ipsilateral (*blue*) and contralateral (*red*)

Europe PMC Funders Author Manuscripts

stimuli of different contrasts (*colour saturation*). Middle column: kernels for contralateral-orienting (*purple*) and ipsilateral-orienting (*orange*) movements. Right column: kernels for reward delivery on correct trials (*cyan*) and white noise on incorrect trials (*black*). Vertical black dotted lines indicate event onset, shading indicates mean ± s.e. across sessions. **c**, Prediction of striatal firing rate obtained from task events, formatted as in (a). **d**, Prediction of striatal firing rate from cortical activity, formatted as in (a). **e**, Trial-averaged activity in each striatal domain (*black*), predicted from task events (*blue*), and predicted from cortical activity (*green*), aligned to stimulus (*red line*), movement (*purple line*), and reward delivery (*cyan line*) (mean ± s.e. across sessions). **f**, Cross-validated explained variance (R^2) of striatal activity predicted from the cortex and task. Small dots, sessions; large dots, mean ± s.e. across sessions; colour, striatal domain. The cortex explains more or the same amount of striatal activity as task events, indicating that striatal activity mirrors cortical activity (signed-rank test, DMS $p = 5.8*10^{-4}$, DCS $p = 0.17$, DLS $p = 0.48$). **g**, Passive responses to visual stimuli in DMS before (*black*) and after (*yellow*) inactivation of VISam with muscimol.

Europe PMC Funders Author Manuscripts

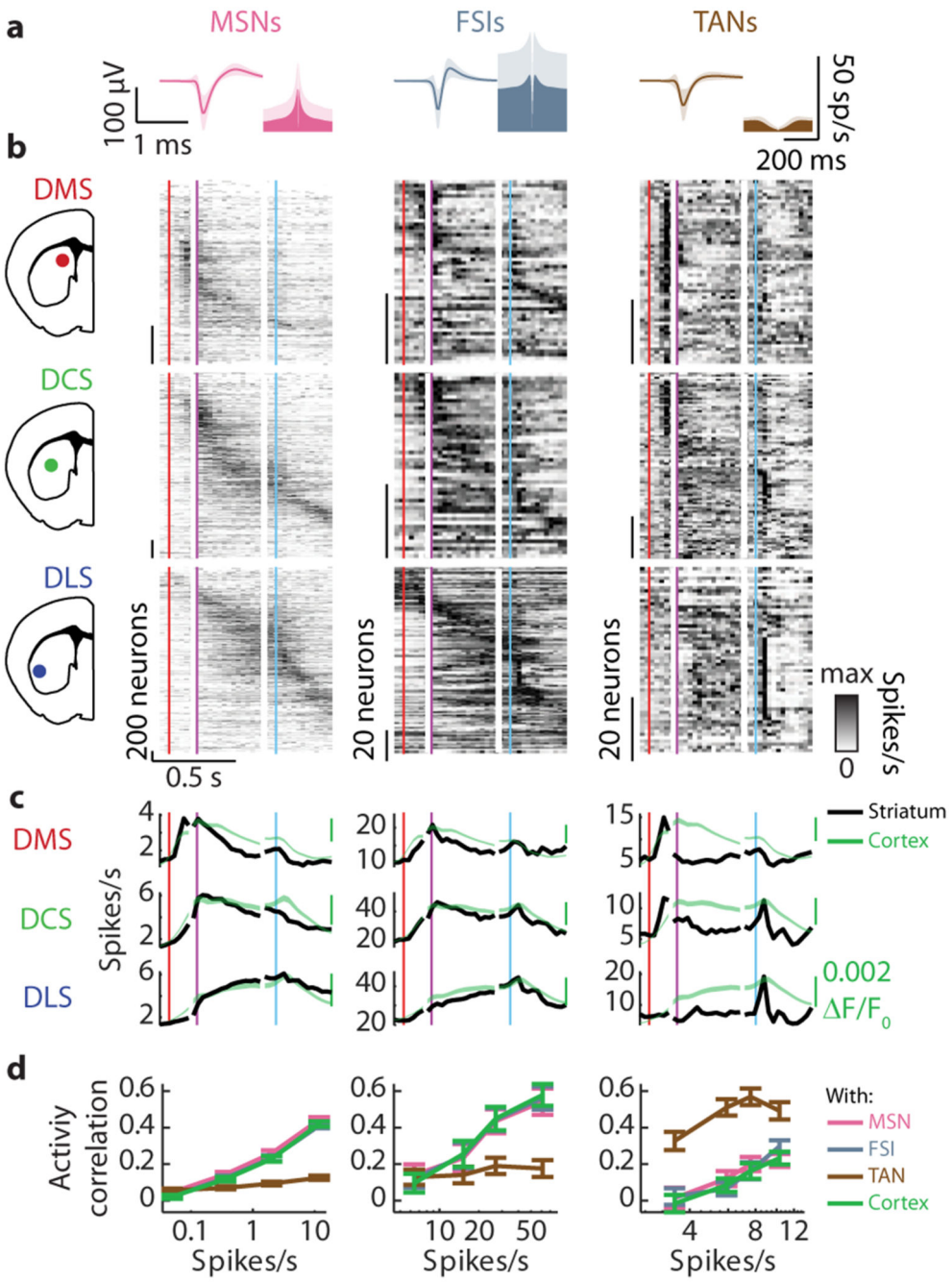

Figure 4. Striatal mirroring of cortical activity is cell-type specific.

a, Spike waveforms and autocorrelelograms for striatal medium spiny neurons (MSNs), fast spiking interneurons (FSIs), and tonically active neurons (TANs) (mean ± s.d. across cells). **b**, Heatmaps showing firing rates of individual cells of each class aligned to contralateral stimuli (*red lines*), contralaterally-orienting movements (*purple lines*), and rewards (*blue lines*), averaged across trials with reaction times < 500 ms, max-normalized, and sorted by time of maximum activity using half of the trials and plotting the other half of trials. Rows correspond to striatal domains: DMS, DCS, and DLS, columns to cell types. **c**, Activity

as in (b) averaged across neurons of each cell type and domain (*black*). For reference, each row reports the cortical activity within a region of cortex associated with each domain (*green*), providing a close match with MSN and FSN activity but not with TAN activity. **d**, Correlations of activity in individual neurons (rows in b) with the average activity of each cell type in the same striatal domain (black curves in c), or with activity of the topographically associated cortical ROI (green curves in c), from non-overlapping sessions to account for interneuron sparsity (mean ± s.e. across sessions). MSNs and FSIs were equally correlated with themselves as with each other (shuffling MSN/FSI labels within sessions, MSN: $p = 0.47$, FSI: $p = 0.99$ across 77 sessions), or with cortical activity (2-way ANOVA on firing rate and type, type MSN $p = 0.94$, FSI $p = 0.88$ across 77 sessions). TANS were correlated with themselves and equally uncorrelated to MSNs, FSIs, and cortical activity (2-way ANOVA on firing rate and type, TAN vs. MSN $p = 7.5*10^{-48}$, TAN vs. FSI $p = 2.0*10^{-6}$, TAN vs. MSN, FSI, and cortex $p = 0.68$ across 77 sessions).

Europe PMC Funders Author Manuscripts

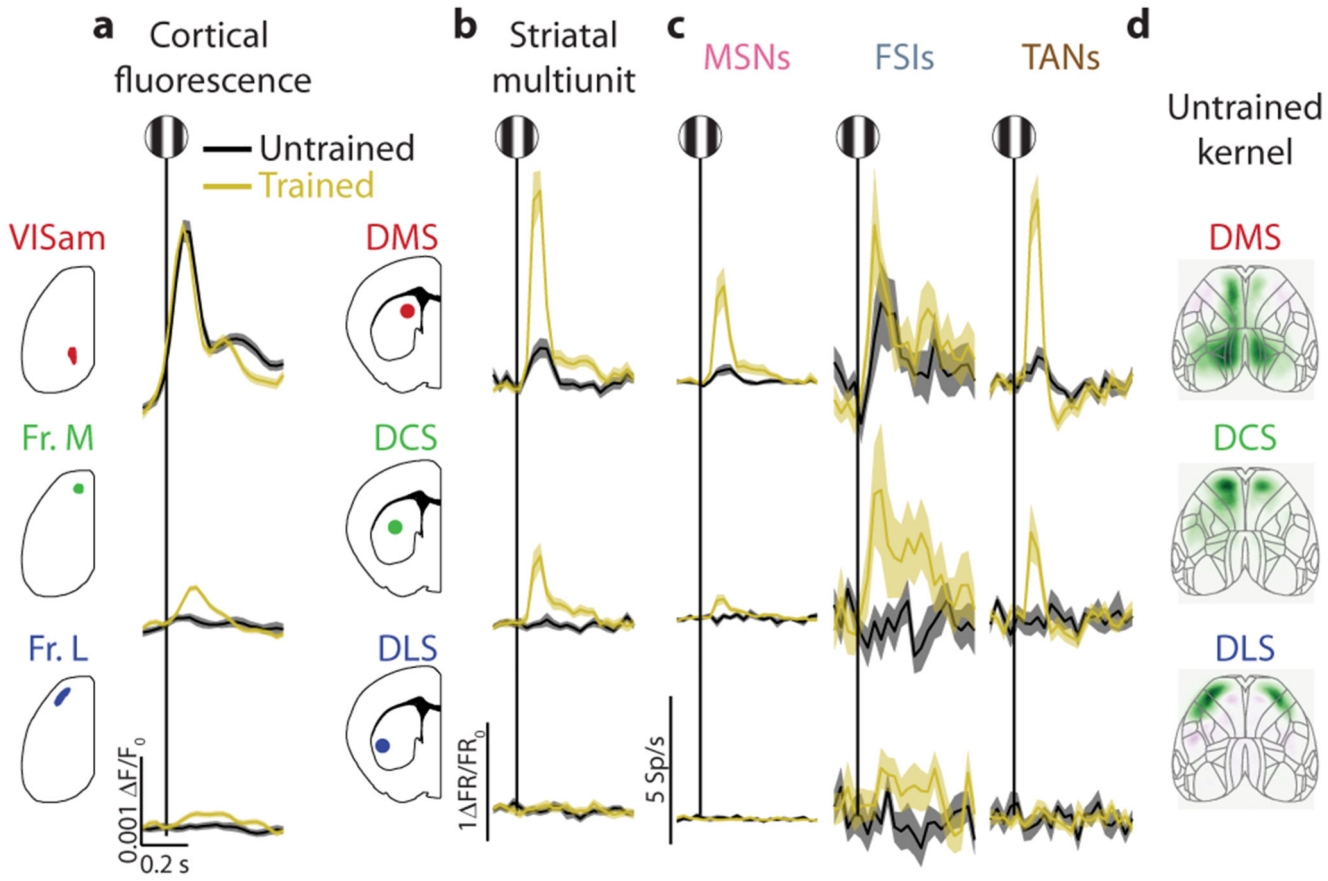

Figure 5. Striatal stimulus responses increase independently from visual cortex after training.

a, Cortical activity within regions associated with each striatal domain in untrained (*black*) and trained (*yellow*) mice to 100% contrast contralateral stimuli (mean ± s.e. across sessions). Stimulus responses in visual area VISam do not change with training, increase in the frontomedial cortex (Fr. M), and are not present in frontolateral cortex (Fr. L) (rank-sum test, VISam: $p = 0.08$, Fr. M: $p = 6.2*10^{-3}$ across 23 untrained and 48 trained sessions, time window 0-0.2 s). **b**, Striatal activity, plotted as in (a). Stimulus responses increase in DMS and DCS (rank-sum test, DMS: $p = 2.1*10^{-4}$, DCS: $p = 9.7*10^{-4}$, time window 0-0.2 s). **c**, Striatal activity as in (a) within each cell type. Stimulus activity within DMS and DCS increases for MSNs and TANs but not for FSIs (rank-sum test, DMS: MSN $p = 2.8*10^{-3}$, FSI $p = 0.32$, TAN $p = 0.013$, time window 0-0.2 s). **d**, Cortical kernels for each striatal domain computed from untrained mice passively viewed visual noise (as in Fig. 2g). Average domain kernels for each mouse are equally correlated across trained mice as they are between trained and untrained mice (rank-sum test $p = 0.65$).